Anion Photoelectron Spectroscopy and Ab Initio Calculations of Asymmetric Halogen Dioxides

Peter Watson

Supervisor: Dr Duncan A. Wild

Honours Thesis submitted as part of the B.Sc. (Hons) degree

The School of Chemistry and Biochemistry

The University of Western Australia

Date of submission: 08/05/15

Declaration

I certify that the substance of this thesis has not been previously submitted for any degree or diploma and is not currently being submitted for any degree or diploma.

I certify that, to the best of my knowledge, any help received in preparing this thesis, and sources used, have been acknowledged in the thesis.

Peter Watson, May 2015

Acknowledgments

The past year has presented me with an interesting and challenging experience and it goes without saying that I am indebted to several people. First and foremost, I would like to thank my supervisor Dr. Duncan Wild. Not only for all the guidance, help and advice I have received over this project but also for making working towards this thesis as enjoyable as it has been. Working in the lab feels more like tinkering in a back shed and is something I could do for years to come.

Thank you Prof. Allan McKinley for kindly providing us with a source of oxygen.

Many thanks to the staff of the Mechanical Workshop of the School of Chemistry and Biochemsity for the maintenance of the TOF-PES and primarily the rotary pumps during this project.

To the other members of the Wild group for discussion throughout the year. Being dropped into the deep end of Linux, LaTex, Gaussian 09, CFOUR and a host of other programs was always a daunting prospect and I must thank Marcus Kettner and Chia-Yang Lim for their help in the early days of this transition. Richard-Bentley Moyse and Duncan Beckham thank you for providing a template from which to build this thesis. Also to Marcus for all the Drum and Bass mixes he has played in the office and for always being courteous and turning down the volume when I came in when he thought I didn't like it.

Abstract

Ab initio calculations have been conducted of halogen-oxygen neutral and anion complexes for bromine and iodine. The purpose of these calculations is to determine their geometric and electronic structure. To support these calculations, anion photoelectron spectroscopy has been conducted on the halide-oxygen complexes with good agreement between experiment and calculation. The classification of these complexes could have implications to current atmospheric models and results suggest that these complexes are stable in both forms, however their stability is low and would hence exist in low concentrations in atmospheric conditions.

Contents

List of Figures

Chapter 1

Introduction

This chapter aims to discuss the background of the techniques to be used in the experiments, being photoelectron spectroscopy and the ab initio theoretical methods used for the accompanying calculations. A more detailed discussion of the apparatus used for the experiments follows in Chapter 2. The second aim of this chapter is to place the work in context and will detail previous work conducted on similar species as well as the impact of the work in regard to atmospheric chemistry. Finally the specific aims of the project will be put forward.

1.1 Photoelectron Spectroscopy

One of the most powerful techniques used in modern experimental physical chemistry is spectroscopy. It offers an avenue to examine the properties of chemical species; all of which are derived from their geometric or electronic structure. Spectroscopy is the wavelength specific light driven change in the structure, and one form includes the ejection of electrons from the bounds of the chemical system. If the target is a stable anion species, then the technique is termed anion photoelectron spectroscopy (PES), and was first used to determine the electron affinity of helium in 1967.[1] This demonstrated the technique as a powerful tool for the determination of these values, and lead to its widespread use.[2] The coupling of other experimental apparatus with photoelectron spectroscopy, for example mass spectrometers, opened areas of chemistry that could not previously be elucidated. For example characterisation of weakly bound systems, most notably work from the groups of Lineberger,[3] Neumark,[4–9] Bowen,[10] Wang,[11] Kaya,[12] and Johnson.[13] The Wild group at UWA has previously studied clusters between halogens anions and carbon monoxide and the technique has proved effective probing these types of species.[14–16]

Photodetachment PES, with which we concern our work here with, works on a basic principle regarding the conservation of energy. The anion state, lying lower in energy for similar geometry than the neutral state, is excited by a monochromatic laser.[1] As the energy of the photons is known, and provided that it is sufficiently high it can promote the system from the anion state up to one of the vibrational and rotational energy levels of the ground neutral state with excess energy being carried by the ejected electron. It is also possible that low lying excited electronic states of the neutral might be accessed. In changing the electronic structure of the system the electron is ejected from the anion with the difference in energy between the incident photon and the gap between the two states being expressed as the kinetic energy of the photoelectron. This is shown schematically in Figure 1.1, which also demonstrates that vibrational structure can be seen in these spectra provided the resolution of the spectrometer is adequate. Probing the system with a photon of energy only slightly higher than the excited state allows for the production of slow moving electrons. This technique is referred to as anion-ZEKE (zero electron kinetic energy) spectroscopy. Reducing the kinetic energy that the photoelectron carries can increase resolution of the recorded spectra to $1.5\,\mathrm{cm}^{-1}$ by minimising the spread of their velocity distribution.[2,17]

It is important to note that the photoelectron spectrum is a statistical histogram counting the number of electrons in intervals of a time of flight. Regarding the excitation and ejection of a photoelectron as a single event the spectrum is made up of

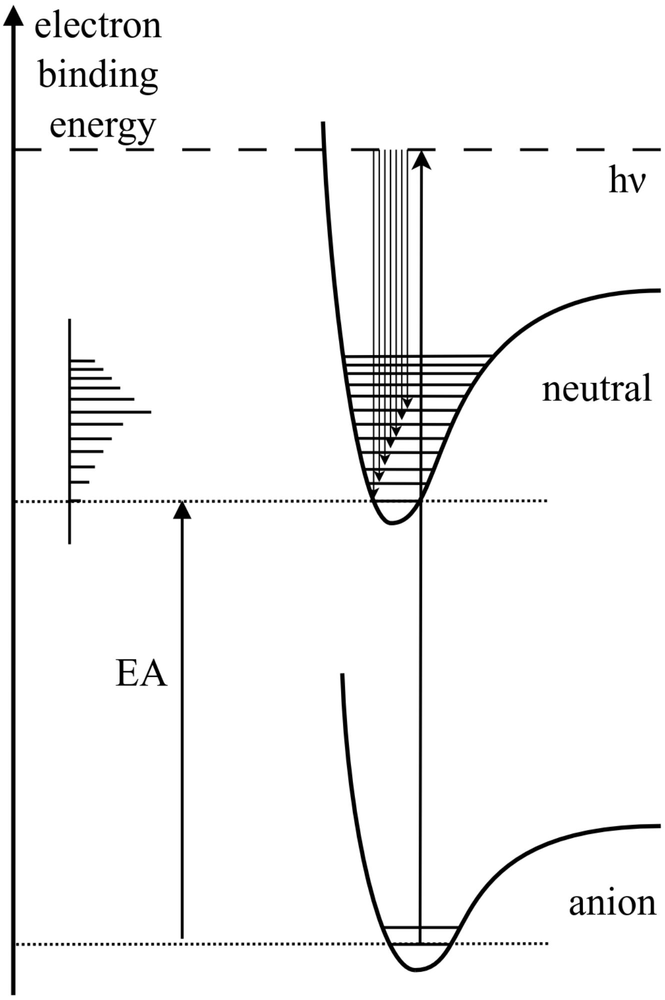

Figure 1.1: Transitions in photodetachment anion PES

the statistical accumulation of these ejections where the degree of overlap of the two wave functions of the final and initial state determines the probability that a given ejection will result in a transfer to that state according to the Franck-Condon principle.[18] The differences in the probability of a given transition determine the relative proportions of photoelectrons that carry a particular kinetic energy and hence the time of flight of these photoelectrons between the point of intersection with the laser pulse and the electron detector. This then appears in the spectrum as the intensity of that transition, with more probable transitions appearing with higher intensity.

A resolution loss and broadening of the PES can come from both quantum and classical effects. The Heisenberg uncertainty principle[19] relates the uncertainty associated with the energy of a state with the lifetime of that state, shown in the equation below (1.1). As the inequality suggests a state whose lifetime is short would lead to a larger uncertainty in energy which would ultimately lead to uncertainty in the kinetic energy of the photoelectron and broadening of the spectrum.[20] With regard to physical effects, the separation of the packet of anions which is pulsed injected, their velocity parallel to the photoelectron flight tube and the direction of the photoelectrons being ejected gives the photoelectrons variations in their flight times and this variation also appears as broadening. It should also be noted that PES experiments are conducted at low pressures as to minimise the interaction between gas particles. Pressure broadening can occur at higher pressures in which molecules in excited states are de-excited by collisions with ground state molecules by dispersing vibrational energy through the gas mixture and leading to uncertainty of the initial state.[21]

As mentioned previously the use of other experimental techniques in conjunction with PES allowed spectroscopy of new novel systems. The technique considered in this thesis is mass spectrometry as it allows for the separation of ionic species in the gas phase based on their mass to charge ratio. In coupling these instruments together the generation of the charged particles, here anions for the PES, is a crucial step, and can be done in a variety of ways. Attachment of electrons to a neutral species is one such method. These electrons can be sourced from a filament that acts as a thermionic electron source that can eject electrons when a negative potential electric field is applied.[14] They can also be generated as photoelectrons themselves by irradiating a metal with laser pulses of energy just higher than the metals work function.[22] Even rudimentary sources such as beams of electrons from a television electron gun can suffice.[1]

$$\Delta E \Delta t \geq h \tag{1.1}$$

Once the anions have been produced they can be manipulated by electric fields. They are accelerated by the application of a negative potential and the mass to charge ratio allows for separation of the different ions in a gas mixture. Subsequently, these packets of ions can be intercepted by pulsed laser light to detach the photoelectrons and produce the PES. A schematic of a typical PES coupled with a mass spectrometer is shown in Figure 1.1.[17] In the example shown the electrons required for anion production are produced by a laser detaching electrons from a rotating metal rod and then introduced into a pulsed gas beam leading to ionisation. The adiabatic expansion of the gas pulse is then passed through a conical shaped skimmer that collimates the beam. This adiabatic expansion is important as it cools the species and minimises interactions that could lead to collisional (pressure) broadening described previously.[21] Mass separation is achieved in the flight tube running along the x-axis shown here and the photoelectron flight tube runs perpendicular to that.

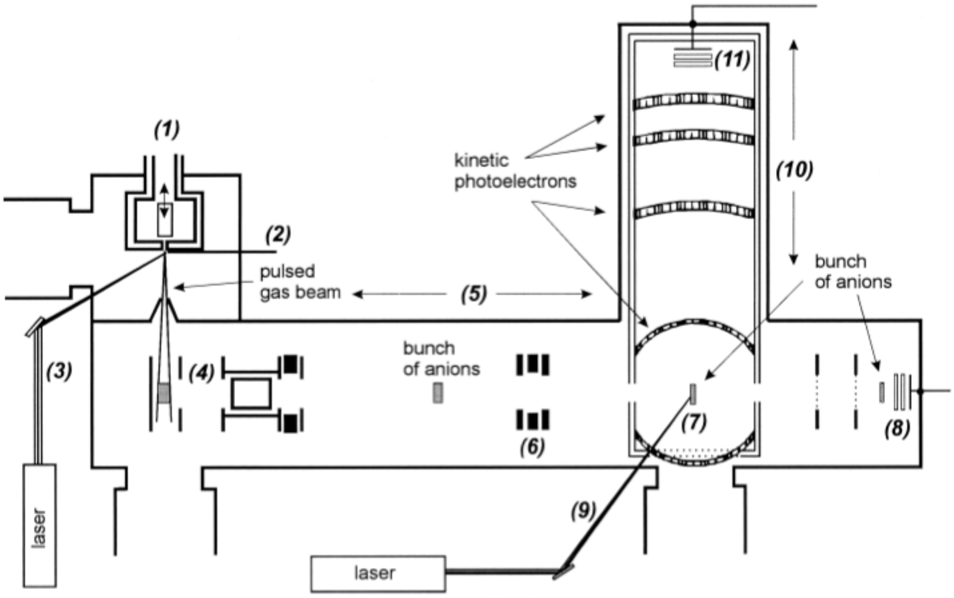

Figure 1.2: Schematic for a PES coupled to mass spectrometer[17]

1.2 Computational Methods

Computational methods are used to explore potential energy surfaces of molecules. A potential energy surface is a map of potential energy of the system versus the geometry. An example of one dimensional potential energy surfaces has been shown previously in Figure 1.1. The purpose of describing these surfaces is that they allow the motion of the nuclei to be predicted because the force on the nuclei is determined by the gradient of the surface at that point.

Ab initio calculations are one such computational method of describing a chemical system. They are based on quantum mechanical methods and utilise only fundamental constants. These methods provide approximate solutions to the Born-Oppenheimer approximation of the many body Schrödinger equation (1.2) to the highest degree of accuracy. The impetus behind computational chemistry is then to determine the energy associated with a molecule, including its electron correlation energy. The methods on which focus is placed here are the Hartree-Fock (HF), Møller-Plesset second order perturbation theory (MP2) and coupled cluster theory with singlets, doublets and approximated triplets (CCSD(T)).

$$\widehat{H}|\Psi\rangle = E|\Psi\rangle \tag{1.2}$$

1.2.1 Hartree-Fock Theory

In quantum mechanical methods, the Schrödinger equation includes the Hamiltonian operator on the wave function that describes the particles energy, both kinetic and potential. Use is simplified through application of the Born-Oppenheimer approximation that states that the nuclei are essentially stationary relative to the electron. This is also the approximation that allows for the production of potential energy surfaces. The problem is simplified somewhat by approximating the kinetic terms of the nuclei.[23] From here only the interaction between the electron and the nuclei and between electrons need be considered. Introducing an electron, the energy of this simple system can be calculated, however systems with many electron systems become extremely complex very quickly. To avoid this the effect of this electron is then approximated to a mean field that surrounds the nucleus and rather than try and calculate the interaction of a second introduced electron with the first at all possible positions, only the interaction with the mean field of the preceding electrons is calculated.[24] This is the essence of the Hartree-Fock method, in which every electron experiences the mean effect of every other electron in the system.

As such the Hartree-Fock form of the wave function becomes an antisymmertized product of functions $\chi(x)$ called molecular orbitals which are linear combination of atomic orbitals, or the Slater determinant (1.3), where x represents these variables (position and electron spin). Roothaan demonstrated[23] that the atomic orbitals could be combined to make up the molecular orbitals with expansions coefficients appropriately applied to each function. Computationally this allows the calculation for the electronic wave function by making a guess for these coefficients and then solving the Hartree-Fock equations for the energy and a new set of coefficients. If the change in these coefficients is sufficiently small depending on the criteria specified then the wave function is deemed to have converged. If not these new coefficients are used as a new guess and the process iterates until convergence.[24]

$$\Psi(x_1, x_2, \ldots, x_N) = \frac{1}{N!} \times \begin{vmatrix} \chi_1(x_1) & \cdots & \chi_N(x_1) \\ \vdots & \ddots & \vdots \\ \chi_1(x_N) & \cdots & \chi_N(x_N) \end{vmatrix} \tag{1.3}$$

The Hartree-Fock method described above accounts for a large percentage (98%) of the energy associated with a molecule. However by treating the electrons as a consistent field with which the other electrons interact it ignores the fact that they are discrete particles and it does not account for electron-electron correlation energy,[25] being the energy associated with the instantaneous electrons repulsion. Often this energy is very small when compared to the total energy, for example only 0.5% in a water molecule[24] however can be comparable in size to other energies that determine chemical interaction for example electron binding energies.

The following sections will discuss computational methods for including electron correlation, and in the case of Møller-Plesset perturbation and coupled cluster methodologies, the reference wavefunction is based on the Hartree-Fock procedure discussed above.

1.2.2 Møller-Plesset Perturbation Theory

Møller-Plesset second order perturbation theory is one such method to account for electron correlation and is a special case of Rayleigh-Schrödinger perturbation theory.[26] In perturbation theory the true Hamiltonian is defined as the combination of an unperturbed Hamiltonian and the applied perturbation. From this a power series in some coefficient of the perturbation of energies and wave function can be derived and the order at which this series is treated is considered the order of the perturbation (for MP2 this is second order).[24]

$$\widehat{H} = \widehat{H}^{(0)} + \lambda \widehat{V} \tag{1.4}$$

MP2 calculations have been shown to account for 92.4% of the total correlation energy on average for a variety of molecules (percentage correlation accounted for ranging from 82% to 98%).[27] Higher order calculations can be attempted in Møller-Plesset perturbation theory and they have shown an increase in the percentage of correlation energy recovered.[28] However it has been shown that at higher order, the percentage of the correlation energy accounted for by Møllet-Plesset theory decreases. A plot of this is given in Figure 1.2.2 based on data by Christiansen[29] in which calculations were done involving a single neon atom as a relatively simple multi-electron system. This work is an extension of that done by Handy and Somasundram[30] in which they considered the suitability of MP theory at up to 48th order with calculations regarding water, however as can be seen in Figure 1.2.2, the divergence only becomes more pronounced beyond this point.

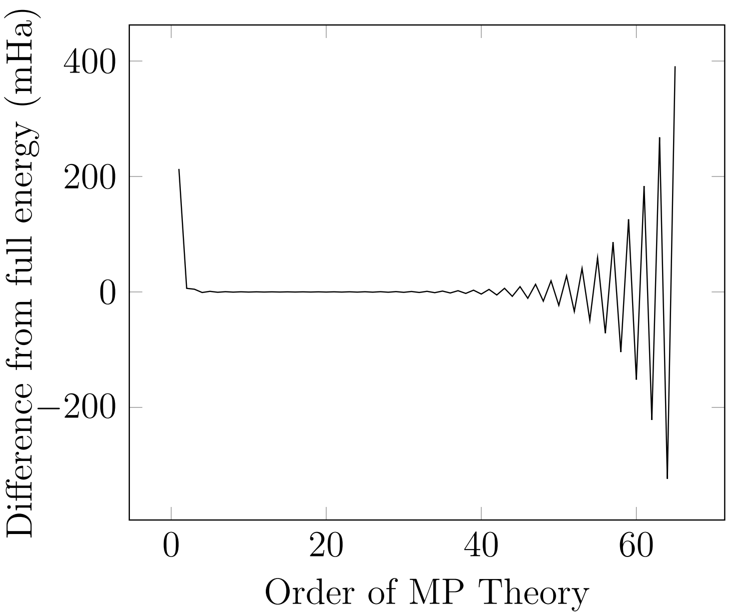

Figure 1.3: Plot of divergence of MP energy at higher order for Ne atom[29]

1.2.3 Coupled Cluster Theory

Another method for incorporating electron correlation energy into the calculation is coupled cluster theory.[31] It does this by exciting electrons from a ground state to and excited state and considering these energies by applying a cluster operator to the wave function of the electrons as well as applying the Hamiltonian. In the full calculation all electrons are excited all unoccupied orbitals. This becomes unfeasible so the calculation is stopped at a certain number of excitations and is where the denotation CCSD(T) with which we consider here originates. CCSD(T) indicates the calculation involves coupled cluster theory with single, double and approximated triple excitations. Much like the order of calculation can be increased in Møller-Plesset perturbation theory so can the number of excitations be increased in coupled cluster theory, however increases in the required computational demands usually outweigh the increases in accuracy that they provide. Considering a water molecule as a test case, CCSD(T) accounts for 99.71% of the total correlation energy.[28] It is also advantageous in investigating the whole potential energy surface in that in comparison to Møller-Plesset perturbation theory this percentage of electron correlation energy accounted for does not decrease substantially as bond length is increased (only 0.5%).[28]

1.2.4 Density Functional Theory

It has been established that CCSD(T) currently sits as a "gold standard" method for energy calculation in computational chemistry with respect to other ab initio techniques. It should also be compared against predominantly empirical methods also, namely density functional theory (DFT).[32] DFT describes the energy as a function of electron density (1.5) rather than of the wave function, and utilises this density function to calculate the electronic energy of the system. This energy expression contains the interaction between the electrons and the nucleus and electrons with each other as a potential and a kinetic energy term for the electrons, all as functions of the electron density.

$$\rho(r) = N \int \cdots \int |\Psi(r, \omega_1, x_2, , x_N)|^2 \mathrm{d}\omega_1 \mathrm{d}x_2 \cdots \mathrm{d}x_N \tag{1.5}$$

DFT offers a method that is much faster than the MP2 and CCSD(T) ab initio methods discussed previously, and since it is about the same accuracy as MP2, has become widespread in calculating many electron systems. As mentioned previously the benefits of speed compared with acceptable accuracy are weighed in choosing an appropriate computational method.[33] With the cases dealt with in this thesis, the preference is made for accuracy as we can afford high level ab initio methods in our relatively simple systems with a limited number of atoms. DFT also has proven inaccurate in characterising species similar to the ones we investigate. Alcami[34] showed that a high level of spin contamination in DFT (and some ab initio methods such as MP2) as a result of the longer bond lengths in asymmetric halogen dioxide radicals lead to spurious results. Calculations gave potential energy surfaces that were uncharacteristic of similar species and determined values of harmonic frequencies that differed greatly from experimental data.

The remaining sections will discuss firstly, the role ozone plays in atmospheric systems and the way that halogen containing compounds impact atmospheric ozone concentrations. Secondly, previous work undertaken on systems similar to those in this thesis will be discussed to place this work into context.

1.3 Ozone and Atmospheric Chemistry

Ozone is known to play an important part in atmospheric chemistry, and primarily does this in two ways: by absorbing ultra-violet wavelength radiation in the atmosphere and initiating important atmospheric reactions. Ozone absorbs radiation around 255 nm quite strongly with an absorption coefficient of approximately $140\,\text{cm}^{-1}$.[35] It does this to such a great degree that even in small concentrations; most of the radiation to which the Earth is exposed is blocked, providing protection for those living on the planets surface.[36] Current measurements of atmospheric ozone of what is known as the Antarctic ozone hole are between 120 and 220 Dobson units (3rd October and 22nd December 2010) and the area over the southern half of Australia ranges between 275 and 325 DU. The ozone hole is represented in Figure 1.3.[37–39]

These measurements are reported by the CSIRO but were taken by using the Earth Observing Satellite (EOS) Aura that utilises differential optical absorption spectrometry (DOAS). It is important to consider, particularly with ozone measurements over Australia that the Dobson unit is defined as the thickness in micrometres that the ozone in a column of air would be when compressed down at 0° and 1 atm

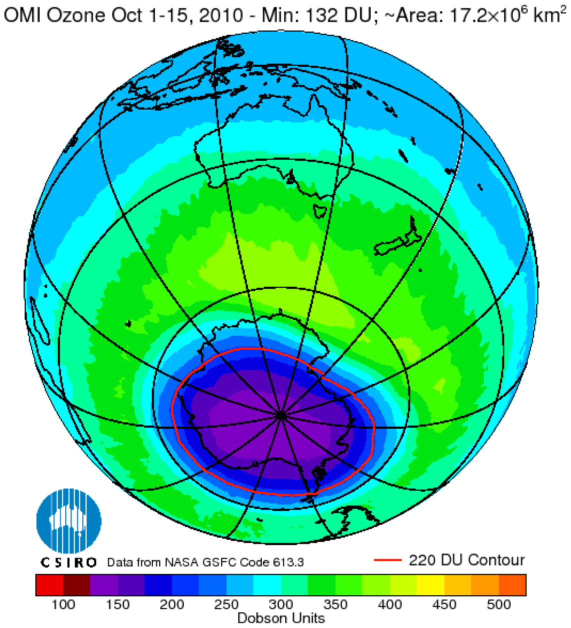

Figure 1.4: The ozone hole over the Antarctic. Measured in Dobson Units

of pressure. The ozone that primarily concerns us is stratospheric and urban ozone while measured by DOAS and reported as part of the atmospheric column supplements this ozone. Hence considering ozone measurements from non-urbanized areas allows us to gauge levels of stratospheric ozone with the trade-off of somewhat ignoring the urban environment as a source of halogen species.

With respect to the public health issue related to decreased ozone levels. It is widely accepted that prolonged exposure to ultra-violet radiation of wavelengths less than 350 nm can significantly increase the risk of skin cancers, cataracts and a range of other diseases in humans.[40] The formation of melanin and the thickening of the epidermis layer of the skin are mechanisms by which the body protects itself from UV exposure, but damage is still done to the DNA within the skin cells and irradiation over a long period of time can cause these abnormalities to accumulate and replicate, forming cancers.[41]

Ozone can undergo photolysis when excited by ultra-violet light of 290 nm and generates O_2 and an oxygen atom radical that acts as an initiator.[42] This initiation is often indirect by the oxygen radical reacting with water molecules to produce two hydroxyl radicals that then go on to initiate atmospheric reactions. Although this appears to suggest that there is a loss of ozone the complex set of competing reactions results in the destruction and reformation of ozone giving a zero net loss overall.[43]

In 1974, Molina reported a possible mechanism by which halogenated compounds, chiefly chlorofluorocarbons (CFCs) that had been released into the atmosphere after their use as refrigerants and aerosols, were depleting ozone concentrations:[44]

$$\mathrm{Cl} + \mathrm{O_3} \longrightarrow \mathrm{ClO} + \mathrm{O_2}$$
$$\mathrm{ClO} + \mathrm{O} \longrightarrow \mathrm{Cl} + \mathrm{O_2}$$

The key aspects that were demonstrated by this paper were that the CFCs released into the atmosphere were chlorine sinks that were activated by ultraviolet radiation in the stratosphere to release chlorine atoms and that these were acting catalytically to produce a net loss of ozone in the atmosphere. Although the role of chlorine in ozone destruction was known for some time,[45] prior to this work the amount of CFCs being released into the atmosphere and the photolytic reaction of CFCs to produce chlorine was underestimated and as such existing models were proven inaccurate.

The mechanism proposed above was tentatively used to guide other atmospheric studies and improve models of the time.[46] However as part of its study the role of chlorine oxide radicals were investigated with respect to their relative abundance, structure and the role they played in the above reactions with respect to both kinetic and thermodynamic stability.[47] However, this mechanism was later expanded on by Vaida.[48] In this work the importance of chlorine oxide and chlorine dioxide as intermediates in the destruction of ozone was established and the photoreactivity of these investigated by both photoelectron spectroscopy and calculation. The reactions illustrating chlorine oxides interaction with ozone are as follows:

$$\mathrm{ClO} + \mathrm{O_3} \longrightarrow \mathrm{ClOO} + \mathrm{O_2}$$
$$\mathrm{ClOO} \xrightarrow{\mathrm{M}} \mathrm{Cl} + \mathrm{O_2}$$
$$\mathrm{Cl} + \mathrm{O_3} \longrightarrow \mathrm{ClO} + \mathrm{O_2}$$

Where the species M is some mediating or buffering species.

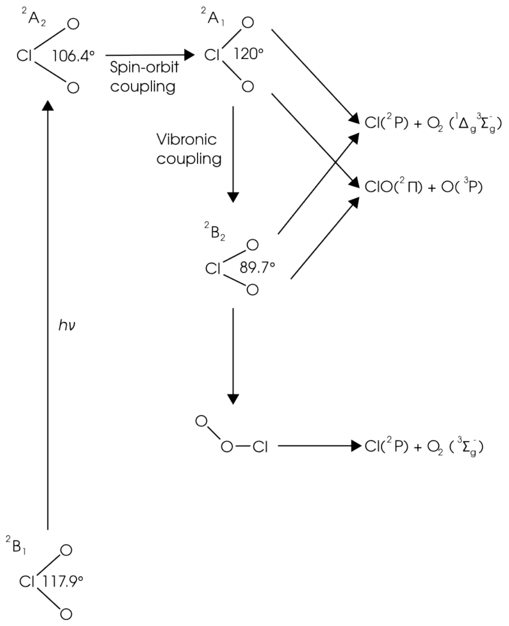

Figure 1.5: Photoreactivity of ClOO adapted from Vaida[48]

What this new mechanism shows is the transformation of two ozone equivalents to three oxygen equivalents. Also in this work Vaida illustrates the photo-reactivity of one of the species in this reaction (chlorine dioxide) and how its photo-reactivity impacts on the products that are produced, shown in Figure 1.5. Chlorine dioxide is excited from the $^2B_1$ state to the $^2A_2$ state. Spin-orbit coupling results in the chlorine dioxide to transition to the $^2A_1$ state from which it can degrade to give various products shown or undergo vibronic coupling to the $^2B_2$ state. The same products are still available to this state or the molecule can isomerise to give an asymmetric chlorine dioxide. The overall yields of this system are determined by the kinetics of each of the reactions, including those that are photochemical and electronic, but the importance of asymmetric chlorine dioxide is seen as its structure (which it should be noted was not determined unlike the other symmetric isomer) and energetics affect the overall products of chlorine-ozone interactions.

In previous literature there is much work reported concerning chlorinated compounds compared with the other halogens bromine and iodine. However brominated and iodonated species are much more reactive than chlorine and still contribute to stratospheric ozone depletion.[49] Work regarding bromine as a part of atmospheric chemistry has paralleled work on chlorine. Bromine radicals were detected in the stratosphere in 1975 and following this, mechanisms for their interaction with ozone were postulated and attempts were made to quantify the effect they had on ozone destruction.[50] It was shown that although concentrations of bromine radicals were low (approximately 10^{-11} (v/v)) they contributed a 0.3% loss in the global ozone budget. It was suggested also that this figure would only increase with increased concentrations of bromine. Anthropogenic sources of bromine have in the past included leaded fuels as anti-knock fluid and more recently from use as flame-retardants and in agriculture as fumigants.

As with research on atmospheric chlorine, the focus later shifted to bromine oxides rather than the radicals themselves as these represented the intermediates of the reactions that were being investigated. In regard to atmospheric chemistry their detection and impact on ozone was the main concern. It was shown that bromine oxide can play a role by reacting with chlorine oxide to form bromine dioxide and a chlorine radical or chlorine dioxide and a bromine radical that can go on to initiate further ozone destruction.[51,52] Both bromine oxide and bromine dioxide species have been detected in the atmosphere,[53–55] however they are kinetically unstable and exist in low concetrations. This has contributed to difficulties in their detection using spectroscopy in the past.

1.4 Halogen Oxides and Dioxides

Having established the significance of halogen chemistry in the depletion of stratospheric ozone and importance that stratospheric ozone in mediating UV exposure to the planet, previous work regarding the characterisation of halogen oxides and dioxides both theoretically and experimentally is to be discussed more specifically.

Bromine dioxide has been investigated extensively in recent decades, however work has primarily involved characterising the BrO_2 radical. It is clear that permutations of this compound can exist in two different isomers; the symmetric OBrO and the asymmetric BrOO. As discussed previously the significance of these two isomers is relevant in the photo-isomerisation reactions and subsequent atmospheric interactions. Unrestricted second order Møller-Plesset perturbation was used with effective core potentials and TZ(2df) basis sets to optimise the geometries for these isomers[56] giving Br−O bond lengths of 2.291 Å, and 1.650 Å, for the asymmetric and symmetric respectively. The BrOO angle and the O−O bond length in the asymmetric isomer was calculated to be 116.4° and 1.214 Å, and in the symmetric isomer the OBrO angle was found to be 114.9°. Additional energy calculations completed at CCSD(T) level of theory on these geometries yielded heats of formation that showed good agreement to experimental values with smaller associated error.[57]

These two geometries show a significant increase in the Br−O bond length in the asymmetric BrOO and demonstrate that BrOO can be classified as a more strongly bound van der Waals cluster based on a definition of the van der Waals bond length being in the 2-5 Å range.[58] Utilising the same working definition the symmetric OBrO and bromine oxide[59] are both strongly chemically bound and not van der Waals clusters. With respect to the atmospheric reactions that these species take part in, the van der Waals clusters which feature longer bond lengths could represent the entry and exit pathways of the reactions describing bromides interaction with ozone and exploration of this potential energy surface could support this. The anion species have also been investigated computationally for the symmetric OBrO and BrO.[60] In general the bond lengths increase moving from the neutral to the anion, which is to be expected and could suggest similar trends to occur in the asymmetric BrOO.

Experimentally, extensive work has been carried out on the BrO_2 and BrO radicals. The symmetric dioxide has been investigated via rotational spectroscopy[61] that provided geometric data, photoelectron spectroscopy[62] that added to this data and included electronic structure data and IR spectroscopy.[63] The geometric data is summarised in Table 1.1. Note that in the photoelectron spectra of the $OBrO^-$ the electron affinity determined was 2.515eV.[62]

Table 1.1: Geometric data of BrO_2 and BrO radicals from literature. Associated errors are included where available.

Work	OBrO r (Å)	α(°)	$OBrO^-$ r (Å)	α(°)	BrO r (Å)
Müller[61]	1.644(1)	114.3(1)	–	–	1.721
Wen[62]	1.649	114.4	1.758	111.9	–

In contrast the iodine equivalents of these molecules have not been widely investigated. This is partially due to their significantly lower abundance in atmospheric chemistry.[64] Since first characterisation with UV-vis spectroscopy[65] some experimental work has been carried out, via IR spectroscopy[66] and PES spectroscopy.[67] The work by Gilles[67] determined the electron binding energy of the anion to be 2.577 eV. Although some theorectical calculations have been carried out, they are limited. Misra[68] characterised both the symmetric and asymmetric isomers of IO_2 at the MP2 level of theory, thereby predicting I−O bond lengths of 1.811 Å, and 3.346 Å, and bond angles of 111.4° and 121.0° respectively and an O−O bond length in IOO of 1.219 Å,. Additional calculations by Lee[69] at the CCSD(T) level with the 6-311+G(3d,f) basis set predicted bond lengths of 1.955 Å, in IO and 1.875 Å, in

OIO.

This section concludes with a discussion of previous work undertaken on the chlorine system which is the most prolifically studied, and there is an abundance of information regarding its oxides and dioxides. Grein[70] reports CCSD level calculations regarding ClOO whereby he determined the ClOO anion to have a Cl−O bond length of 3.631 Å, an O−O bond length of 1.201 Å, and a ClOO bond angle of 80.47°. This data are interesting in that the anion has a significantly reduced bond angle to those seen previously; in fact the final geometry is that of a 'Tee' shape. They give an electron affinity of 3.79 eV by comparison with the doublet state of the neutral complex. Irikura[71] supplies geometry data for $ClOO^-$ at CCSD(T) level and classifies the cluster as having three distinct isomers a 'Tee' shape ($^3B_1$), linear ($^3\Sigma^-$) and bent ($^3A''$). The Cl−O bond lengths for each structure are 3.569 Å, 3.410 Å, and 3.432 Å, respectively and the bent structure has a ClOO angle of 96.0° and is deemed to be the optimised geometry having the minimum in energy. Starting from the bent structure optimisation leads to ClOO angles much less, near 80° which is extremely close to the 'Tee' shape configuration, yet Irikura presents harmonic vibrational frequencies for the 'Tee' shape at CCSD(T) level with an imaginary frequency of $11i\,cm^{-1}$ for the bending mode that points towards the 'Tee' configuration being a transition state. Irikura also completed multiconfiguration self consistent field (MCSCF) calculations for ClOO to investigate differences in geometry and energy between the triplet and singlet states of the complex.

Photoelectron spectra of the ClOO,[72] OClO and ClO anions[67] have been recorded previously. Boesl[72] reports values for all three of the chloride species using anion-ZEKE spectroscopy. The high resolution of this technique allowed for vibrational structure as shown in Figure 1.4. Electron affinities of 2.2775(13) eV, 2.1451(25) eV and 3.6600(2) eV are reported for ClO, OClO and ClOO respectively, where here ClOO is characterised as a weakly bound van der Waals cluster. This assignment is

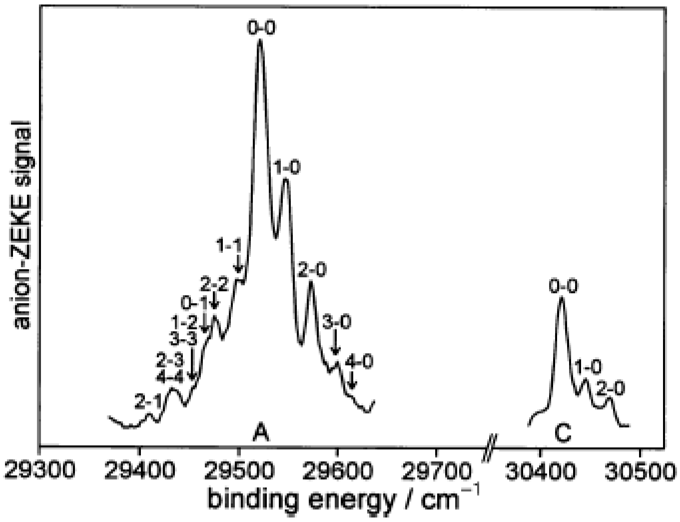

Figure 1.6: anion-ZEKE spectrum ClOO[72]

based not only on the geometry that is calculated for the structure but also the comparison between electron affinities between ClOO and ClAr (3.6594 eV), a species already identitfied as a van der Waals complex. In addition it is noted that the low vibrational frequencies for the Cl—O bending and stretching modes is also indicative of a van der Waals complex.[72]

1.5 Production of Halogen Dioxides and Project Aims

The aim of this project is to explore the potential energy surfaces of the asymmetric halogen dioxides of both iodine and bromine. As described previously, symmetric halogen dioxides can be more readily produced for spectroscopy,[61,63,65,72,73] however production of the asymmetric halogen dioxides has often proved more difficult. In Boesl's work it is reported that ClOO anions were produced for anion-ZEKE spectroscopy by seeding an oxygen-argon gas mixture with CCl_4[72] and it has since been shown that van der Waals clusters with carbon monoxide can be produced in the gas phase by similar methods with equivalent halogen sources such as dibromomethane[15] and iodomethane.[16] This offers a possible method to produce and probe halogen dioxide clusters of bromine and iodine.

By producing these halogen dioxides in an oxygen-argon gas mixture in a similar fashion to the way that ClOO has been produced, mass-selective detection by time of flight mass spectrometry can allow spectroscopy of a variety of clusters including $Br^{-}\cdots Ar$ and $I^{-}\cdots Ar$. Such an approach also allows for experimentation regarding the optimum proportions of the gas mixture to maximise the production of the desired dioxides. Comparison of the binding energies of these clusters with previous experimental data[5] and the corresponding halogen dioxides should provide an understanding of the degree of perturbation that the halogen experiences when complexed with an oxygen molecule.

Furthermore the use of ab initio calculations for each of the halogen dioxides can support experimental analysis and classification of the clusters as van de Waals complexes or otherwise. This can be done by considering, along with the degree of perturbation, the calculated dissociation energies of the neutral and anion complexes and allow for an assessment to be made as to the stability of the complexes formed. By characterising the via halogen dioxides their energies and potential energy surfaces, and ideally the role that they play in atmospheric reactions, be it in the stratosphere or the marine boundary layer, potential entry and exit pathways can be assessed. Discussed previously is the impact that these bromine and iodine dioxides have on atmospheric reactions and evidence[49] would suggest that they are more reactive than the corresponding chlorinated species. However, one could argue as to the actual impact that they have in the atmosphere, being transient species and hence often present in minute concentrations relative to other ozone depleting species. However, the ability to produce these halogen dioxides in the gas phase and to perform spectroscopy on them is novel, especially considering their instability. Should sufficient amount of these clusters be produced, further study can be conducted of clusters with higher order of oxygen clustering much like degrees of micro-solvation.[74]

Chapter 2

Materials and Methods

The following chapter details the methodology undertaken in these experiments. This includes the procedure following in the preparation of the gas mixtures used, details and the reasoning behind the construction of the time of flight and photoelectron spectrometer, details of the specific ab initio calculations undertaken and the way in which both experimental and computaitional data were processed.

2.1 Gas Mixture Preparation

The gas mixture used in the experiments consisted of trace amounts of a halogen source, oxygen, and argon as a buffer gas. The following is a description of gas mixture preparation.

To ensure a pure gas mixture is achieved, pressures within the gas mixing station apparatus are reduced down to approximately 10-20 mTorr with a rotary pump and liquid nitrogen cold trap. The apparatus is flushed with approximately 100 kPa of argon with the aim of displacing adsorbed gases on the interior surfaces followed by further pumping to once again reduce the pressure to 10-20 mTorr.

The bromide and iodide sources used in these experiments were primarily dibromomethane and methyliodide respectively, with some experiments using diiodomethane. Liquid samples of each of these were degassed by a freeze-pump-thaw method and then introduced to the gas mixing apparatus by allowing their vapour to escape into the region of reduced pressure. Initially the gas mixing station allowed for only one of the halogen sources to be used in a gas mixture at a time, however later modifications to the station allowed for two flasks to be connected and both halogen sources used for better calibration of mass and photoelectron spectra. Also, although in later experiments the system was still flushed with argon it was noted that the adsorbed halogen sources on the interior surfaces of the gas mixing station offered increased signal of other ions in the mass spectra, which contributed to both calibration, and identification of other peaks. As such the steel hosing leading from the gas mixing station to the gas nozzle was replaced with Telfon tubing to increase these adsorption effects without compromising the bulk mixture prepared.

Following the introduction of the halogen species to the gas mixture, oxygen was added. Over the course of experiments the partial pressure of oxygen was varied to assess the degree to which it affected the strength of the signal of the halide-oxygen complexes in the mass spectra. Partial pressures of oxygen were approximately 30, 40 and 70 kPa and discussion as to these effects are offered later. However at present note that 30 kPa offered signal of only near 35 mV and this was deemed too weak as the resulting photoelectron spectra had low count rates. The aim of sufficient signal in the mass spectra is to confirm that a sizeable enough ion packet is available in the laser intersection region so that enough photodetachment events occur for measurement.

The gas mixture is then made up with argon to a total pressure of 450 kPa. As the argon is introduced quite quickly from below it is believed that the oxygen or other gas used in the mixture is pushed as bulk to the top of the vessel and that stratification of the gas mixture occurs. To reduce this effect a period of time is required for the gases to equilibrate and properly mix, in these cases this period was at least 12 hours but preferably longer was given (two days) as stabilisation of the gas mixture can be seen in the mass spectra with the growth and decline of the signals of certain clusters over time.

2.2 Details of the TOF-PES apparatus

The Time of Flight Photoelectron Spectrometer (TOF-PES) used in these experiments was built in 2008 by Robert LaMacchia under the supervision of Dr Duncan Wild. A schematic for the machine is shown in Figure 2.1 and consists of three major sections with a fourth constructed but currently still in development. The sections are the ion-molecule complex formation and extraction chamber, the ion flight tube and mass spectrometer and the photoelectron flight tube and detector. The fourth area shown to the left of the Figure is the slow electron velocity imaging (SEVI) flight tube and detector, as it is near completion it will be discussed later regarding the future direction of this work however it was not used in the experiments decribed in this thesis.

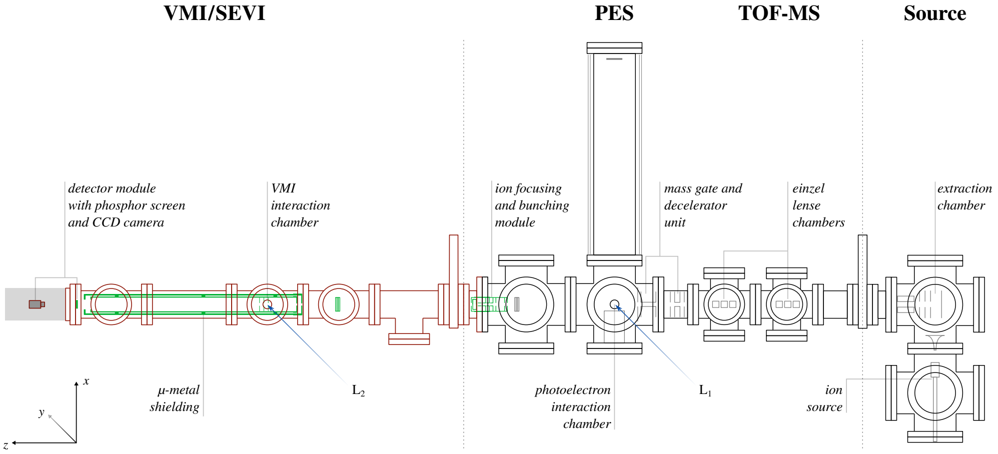

Figure 2.1: A schematic of the TOF-PES apparatus from above. Courtesy of Marcus Ketter

2.2.1 The Extraction Chamber

The ion complex formation and extraction chamber is kept at a vacuum of 1×10^{-8} Torr when not in use and 1×10^{-6} Torr during experiments, with the vacuum being maintained by two diffusion pumps, a Diffstak 250/2000P and a Speedivac E04 which utilized Santovac 5 polyphenol oil to draw 2000L/s and 600L/s respectively. Both pumps are backed by an Edwards E2M40 rotary pump and the Speedivac also features a liquid nitrogen cooled baffle. A manual gate valve separates the ion production and extraction section from the ion and photoelection flight tube sections.

The gas mixture is injected into the source chamber or more accurately allowed to escape the mixing station reservoir by a pulsed solenoid valve. The solenoid is driven by a pulsed circuit (0-500 µs pulse, 0-250 V) to activate an electromagnet and pull a sealing poppet away from the front face of the valve, thereby allowing the gas to exit the valve. A spring behind the solenoid pushes it back into place after the pulse voltage returns to zero. A piezo nozzle similar in design to Proch and Trickl[75] is in development to replace the solenoid nozzle currently being used, and when complete should provide a more reproducable gas pulse with improved gas density per pulse for the TOF-PES apparatus.

The electrons used for the generation of the clusters in this experiment are produced by thermionic emission from a rhenium filament (Goodfellows, Rhenium wire, 0.2 mm diameter). A potential applied to a Wehnelt shield situated behind the rhenium filament generates fast electrons. These electrons are focussed with an Einzel lens to give a small region of higher electron interaction near where the gas is injected. The following reactions show their subsequent interaction with the gas mixture to produce the halide-oxygen clusters.

$$\mathrm{Ar} + \mathrm{e_{fast}}^- \longrightarrow \mathrm{Ar}^+ + \mathrm{e_{slow}}^- + \mathrm{e_{fast}}^-$$

$$\mathrm{e_{slow}}^- + \mathrm{CH_2Br_2} \longrightarrow [\mathrm{CH_2Br_2}]^* \longrightarrow \mathrm{CH_2Br} + \mathrm{Br}^-$$

$$\mathrm{Br}^- + \mathrm{O_2} \longrightarrow \mathrm{Br}^- \cdots \mathrm{O_2}$$

The orifice through which the gas escapes is 0.8 mm. By using a high pressure of the argon backing gas and a small orifice the mean free path of the gas molecules is lowered and the frequency of collisions in the expansion region leads to adiabatic cooling.[76] The internal energy of the molecules is then limited by the binding energy of the clusters. Using a dilute gas mixture, a noble gas can reduce the temperature of the gas mixture and this is why argon is used as a backing gas in these experiments.[77] The injected gas passes through a skimmer that both collimates the ion beam and becomes a fraction of the original gas injected. Overall the use of argon as a backing gas at a higher pressure and the supersonic expansion gives a narrower velocity distribution with velocities closely similar to the backing gas demonstrated in Figure 2.2.[78]

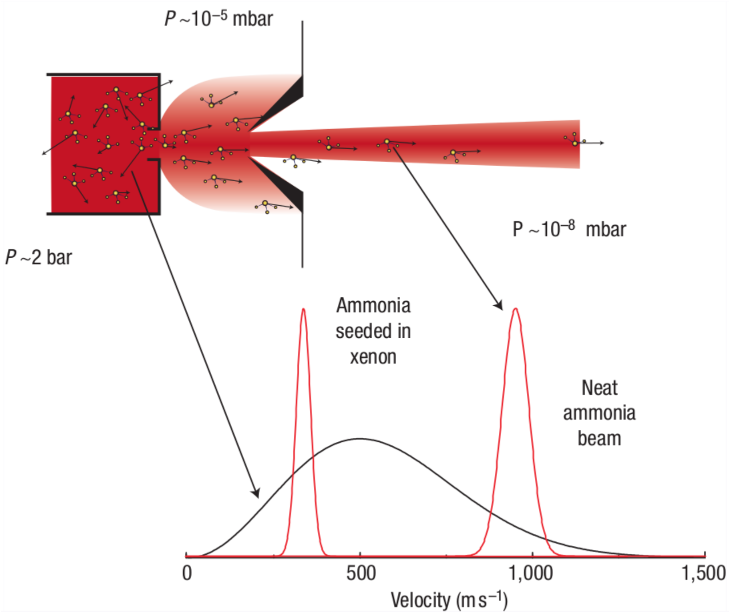

Figure 2.2: The function of the skimmer and the velocity distribution of the gas pulse. [78]

The ion beam drifts through the extraction chamber and enters the region in which it will be accelerated into the ion flight. When it arrives two of the TOF plates are brought to a high negative potential (-1000V) with the leading plate down the flight tube at a ground potential and the centre plate at a slightly lower potential than the back plate to control space focusing. Applying this electric field to the ion beam accelerates only the negative ions along the ion flight tube towards the detector, neutral species remain unaffected and collide with the walls of the extraction chamber and positive ions, are attracted towards the TOF plates and are neutralised upon collision.

Space focusing is an important aspect of the experiments as there is a spread of the ion beam after it passes through the skimmer some whereby particles may be closer or further away from the rear TOF plate. Particles with less distance to travel down the flight tube are subjected to a smaller electric field such that the ion packet arrives at the detector within a narrow time frame. The potential is adjusted based on inspection of the mass spectrum and the resolution of the peaks within it.

2.2.2 The Ion Flight Tube

The amount of kinetic energy given to each of the ions in the ion beam is approximately the same, considering only small fluctuations due to the space focussing discussed previously. Additionally due to the way in which the ions are produced only singly charged ions are created and as a result the time of flight of each ion or cluster along the flight tube becomes dependant on its mass.

Travelling down the flight tube the ion packet can be directed accurately towards the detector by two sets of pairs of parallel plates. The ion beam also experiences a spreading as it travels due to the repulsive interaction of the nearby negative charges. Two Einzel lenses deal with this expansion; each one is made up of three in line metal cylinders with the central cylinder being held at a negative potential and the outer two held at ground. Due to their shape this leads to a focussing of the molecular beam with a focal distance dependant on the voltage applied. In this way the Einzel lenses are electrostatic analogues of optical lenses.

The ions are detected at the end of the flight tube by a microchannel plate detector (MCP, Burle APD 3025MA, 25 mm diameter, 10 µm pore size). This MCP is made up of two microchannel plates: the front plate is kept at a ground voltage while the back plate is kept at 1700 V and the anode for detection is at 1750 V. This design can create a cascade of up to 10^6 electrons with each collision essentially amplifying the signal of the ion beam and allowing for higher sensitivity of detection.[19] An Agilent Technologies DSO6032A oscilloscope, triggered by the leading edge of the potential pulse of the TOF plates, picks up the signal from this detector and time dependant collisions of the ions appear as a spectrum that is then recorded over either 128 or 256 averages.

2.2.3 Laser Intersection and the Electron Flight Tube

In order to record the photoelectron spectrum of the anion-molecule complexes, the ion packet is overlapped with a laser pulse in the presence of a strong magnetic field.

The light source used in these experiments is a Spectra-Physics Quanta-Ray Pro-230, a pulsed Nd:YAG laser. The laser has a fundamental output of 1064 nm radiation at 10 Hz pulse repitition rate, which is then frequency doubled twice to provide 266 nm for photodetachment of the complexes. The maximum power of the 266 nm has been recorded to be 150 mJ per pulse. Nd:YAG lasers, a solid state laser consisting of a neodymium doped yttrium aluminium garnet crystal have been shown to be better at achieving population inversion than other solid state lasers (ie. ruby). This is primarily due to the Nd:YAG laser being a four level system rather than a three level system.[19]

The laser radiation is guided over to the end of the ion flight tube where it is set to intersect the ion packet as it passes through. The angle of the plane polarised light with respect to the direction of the ion beam transit is set by the adjustment of a Glan-Laser polariser, and the power of the beam can be reduced by rotation of a $\lambda/2$ retardation plate immediately before the polariser, thereby avoiding signal saturation. The laser beam is also passed through an aperture and a telescope that reduce the beam diameter to approximately 6mm. The aim of this is to create an optimal beam diameter that is sufficiently large to intersect the ion packet as it passes by (keeping in mind that the ion beam may not pass directly through the centre of the intersection region) but not too large that the positions of photodetachment are too spread and subsequently decrease the resolution of the resulting photoelectron spectra. Additionally, a large cross section yields an increased number of photodetachments that could lead to signal saturation.

Electron collection and detection is based on the magnetic bottle spectrometer devised by Smalley and co-workers.[79] Laser interaction in the strong field of the bottle with the ion packet detaches a photoelectron that follows along the magnetic field lines in a helical motion,[80] which parallelise their paths further down the electron flight tube shown in Figure 2.3. A previous experimental setup utilised an electromagnet to generate the strong magnetic field however due to the high rate of cooling the electromagnet required, and an inability to meet these requirements, the field generated by the electromagnet was prone to deterioration and instability. As such the magnet used for these experiments was a neodymium disk magnet ($Nd_2Fe_{14}B$) that provides a constant and consistent magnetic field. The magnetic bottle has been shown to collect over 98% of the electrons detached by the laser.[79]

In the electron flight tube a weak magnetic field parallel to its length is maintained by passing a current through a copper wire coiled around the exterior, with

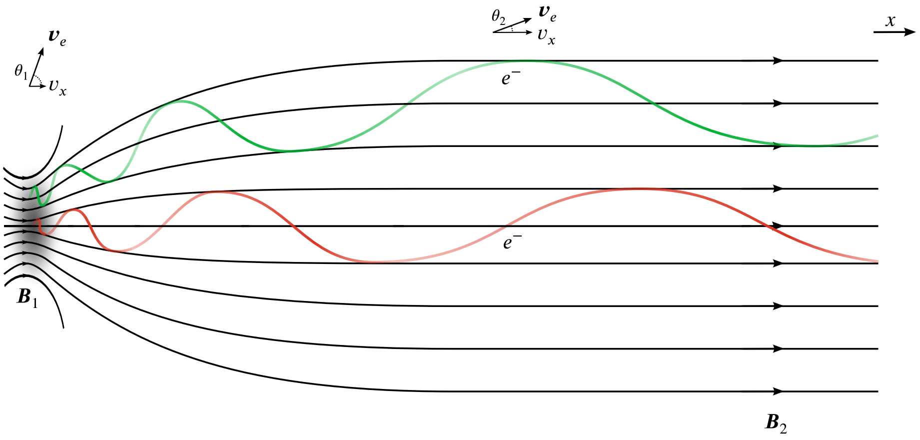

Figure 2.3: Magnetic field lines of the magnetic bottle. Courtesy of Marcus Kettner.

the flight tube being sufficiently wide such that the curvature of the field at its edges has little effect on the photoelectrons roughly centred flight paths. Surrounding the tube and solenoid is a μ-metal shield whose purpose is to attenuate the Earths magnetic field, and other magnetic fields that may be generated from nearby electronics.

At the end of the electron flight tube is situated another MCP for detection of the ejected photoelectrons, in this case a Burle APD 3040MA (40 mm diameter, 10 µm pore size) with the front plate of the MCP held at 200 volt, the back plate at 2300 volt and the collecting anode biased at 2500 volt. In addition there is also a mesh held at ground approximately 25 mm in front of the front plate which creates an electric field to accelerate the slow moving electrons immediately in front of the MCP such that they trigger it without significant effect on their time of flight along the tube. The acceleration accounts for the reduced sensitivity of MCP style detectors for slow moving particles. A VT120A Ortec Fast Pre-Amplifier amplifies the signal detected from the anode; the rise time of all VT120 models is less than 1 ns as such they offer good resolution for use with MCPs in photoelectron spectroscopy. This signal is then digitised by an Ortec Constant Fraction Discriminator (CFD) in combination with a P7888 Fast Comtec GmbH TOF multi-scaler card in 2 ns time bins.

With respect to the timing of the laser it is beneficial to use the peak times of the mass spectrum to infer a suitable period to fire the laser such that it intersects the ion packet. The collection of the photoelectron signal is triggered by the laser hitting a fast photodiode beneath the point it intersects the ion packet and this can be visualised on the oscilloscope. Seeing the temporal location of the laser pulse gives a first step in finding a suitable time to trigger such that it intersects with the ion of interest. Placing the laser pulse before the first ion detected, or in a region free of other ions, is a good start keeping in mind that the laser intersection point is also before the ion flight tube MCP. By connecting the CFD to the oscilloscope the spectrum can be read in real time or at least several sweeps can. By moving forward in time seeing the signal from the first ion allows the timing for that ion to be determined and continuing onwards timings for each ion in the mass spectrum can be recorded in turn provided their signal has enough intensity for PES. Over the course of experimental work a plot can be drawn up that links the mass spectrum detection time with the timing of the laser pulse such as one in Figure 2.4, and this plot can be interpreted to determing good areas to investigate for intersecting a new ion with the laser pulse. Note that some ions have been labelled but not all to avoid over crowding. A summary of the timing elements of the experiment is given in Appendix B (Figure B.1).

The PES spectra are recorded as histograms of electron counts with 2 ns time bins. Although a distribution of photoelectron times of flight are expected, the summation of 10000 laser pulse interactions sees the growth of peaks corresponding in energy to the transitions between the anion and neutral states. Furthermore spectra of the halide-oxygen complexes with which were are interested in were recorded in triplicate for consistency.

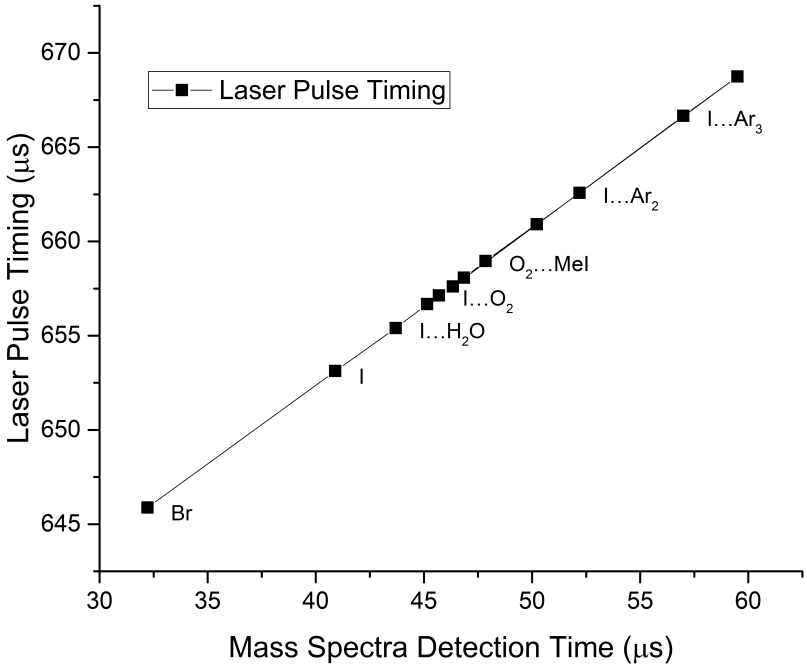

Figure 2.4: A plot of detection time against laser pulse timing.

2.3 Processing of Data:

2.3.1 Analysis of Mass Spectra:

Theoretical values for the times of flight can be calculated based on the settings of the machine and by making a few assumptions as the following derivation shows:

$$E_p = E_k \tag{2.1}$$

$$qV = \frac{1}{2}mv^2 \tag{2.2}$$

$$v^2 = \frac{2qV}{m} \tag{2.3}$$

$$\frac{d^2}{t^2} = \frac{2qV}{m} \tag{2.4}$$

$$t^2 = \frac{d^2m}{2qV} \tag{2.5}$$

$$t = \frac{d}{\sqrt{2V}}\sqrt{\frac{m}{q}} \tag{2.6}$$

In the derivation the largest assumption made is that the ion path is a direct line, that it hits the detector exactly in the centre (the collision point on the MCP is not determinable) and that the beam is unaffected by the einzel lenses when in fact they have a slightly retarding effect. The flight path, d, is not measured accurately for these purposes and as such there is further source of difference here. These calculated values do not offer an exact value due to the assumptions made however they can prove useful in the analysis of the spectra and give general regions in time in which an ion is due to arrive. An example calculation of the TOF of the Bromine-79 isotope anion and assuming a path length of 1.45 m and potential of -1000 V along with constants of the elemental charge, yielded 29.3 µs, which corresponds closely to the time recorded from the spectrum of 32.2 µs.

After a spectrum has been recorded in time of flight, the peaks that are identified easily, in this case the two bromide isotopes and iodide, are used to calibrate the spectrum using the TOF equations and present it as mass units. From here various complexes can be identified by their mass and further calibration can be iteratively performed on the original TOF spectrum to improve the calibration if required. It is important that the peaks in the mass spectra have intensity sufficient enough to indicate that there are enough ions in the packet for intersection with the laser pulse to produce a viable photoelectron spectrum.

2.3.2 Analysis of Photoelectron Spectra:

After a photoelectron spectrum is recorded it needs to be calibrated from time of flight to binding energy. Data treatment of the photoelectron spectra was done using SciDAVis, an open-source plotting program. The basis of calibration is the conservation of energy in photodetachment. The resulting kinetic energy that the photoelectron carries is the difference between the energy associated with the incident photon and the binding energy of the complex and this is given by the following equation:

$$E_k = h\nu - E_B \tag{2.7}$$

Following a similar derivation to the one used in the mass spectra analysis, the kinetic energy of the photoelectron can be show to be proportional to the inverse of the time of flight squared. During experiments calibration spectra of the bromide and iodide recorded to accompany each days set of spectra and the peaks picked from these are shown in the Table 2.1.

Table 2.1: Calibration Data.

		TOF (µs)	σ
Br	$^2\mathrm{P}_{3/2}$	2.5862	0.0129
Br	$^2\mathrm{P}_{1/2}$	3.3680	0.0479
I	$^2\mathrm{P}_{3/2}$	2.2921	0.0078
I	$^2\mathrm{P}_{1/2}$	4.0143	0.0387

Examining this data for calibration the largest standard deviation belongs to the Br $^2\mathrm{P}_{1/2}$ band which is 0.048 µs, corresponding to 24 time bins in the spectrum. These differences are primarily a result of the finding the maxima in the binned data as fluctuations in the electron counts can pose difficulties; smoothing of the spectra first can prove useful here. Considering that the spectrum is made up of 2,500 bins (5 µs), this standard deviation represents less than 1% of the region. As such it is considered that day-to-day differences in the calibration of the spectra are not significant and as such a calibration has been performed over the data set as a whole.

Based on the calibration data above a plot (Figure 2.5) was constructed of the inverse time of flight squared of the peaks corresponding to each electronic energy level of the two halides against the kinetic energies those electrons should carry based on known electron binding energies for these energy levels provided by NIST[81–83] and the wavelength of the excitation laser.

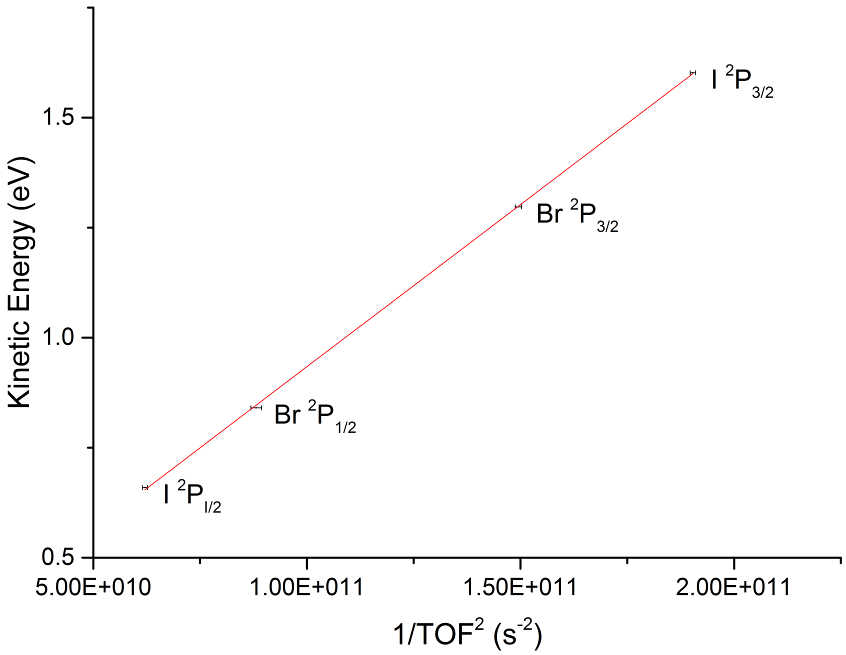

Figure 2.5: The calibration plot used for the conversion of time of flight to kinetic energy in the following analysis.

The calibration curve for these experiments had a gradient of 7.372×10^{-12} eV s^{-2} and an intercept of 0.196 eV. Errors associated with the gradient and intercept are 5.866×10^{-14} eV s^{-2} and 7.772×10^{-3} eV with a regression coefficient of 99.98%. This calibration is applied to the spectra from each day and backgrounds subtracted where appropriate. The spectra are then converted into binding energies based on the energy associated with the laser photon energy, in this case 4.661 eV.

As the spectrum is recorded in time of flight, however is to be presented in binding energy the binned intensities recorded need to be adjusted accordingly using a Jacobi transform. The reason for this transformation is due to the fact that the conversion between the time of flight scale, and energy scale is non-linear. The Jacobi transform can be expressed by following relationship:

$$I(t)\mathrm{d}t = I(E)\mathrm{d}E \tag{2.8}$$

$$I(E) = I(t)\frac{\mathrm{d}t}{\mathrm{d}E} \tag{2.9}$$

By taking the derivative of the kinetic energy with respect to time and substituting it into the above Jacobi transform, the intensities with respect to binding energy can be derived.

$$\frac{\mathrm{d}t}{\mathrm{d}E} = \frac{t^3}{m_e l^2} \tag{2.10}$$

$$I(E) = I(t)\frac{t^3}{m_e l^2} \tag{2.11}$$

Although the path length is not precisely measured, it remains constant and particularly due to other manipulation of the intensities (for example normalisation), its effect is minimal. In this case 1.70 m was used as a straight line from the area of the point of intersection to the detector however that does not take into account the curvature of the path due to the magnetic field or even ejection at an angle although the diameter of the detector would suggest this angle would be small regardless. Note that the cubic nature of the transform leads to amplification of the noise at longer times. Slow electrons would have attributed to them a significant degree of error after the transform is applied. Were a background subtracted the effect of this can be reduced but it still remains significant.

After the Jacobi transform is applied, the triplicate scans for that day are averaged and collected as one spectrum and smoothed using a Savitzky-Golay filter with polynomial order of 3 and a window size of 20. The smoothed spectra for each day are then combined over the period of experiment to produce a single halide-oxygen spectrum from which the binding energies of the two ^{2}P states can be determined.

2.4 Computational Methods:

A series of calculations were carried out to support the experimental data. Based on previous work by Irikura,[71] calculations on the ClOO anion have been replicated in CFOUR using an aug-cc-pv(T + d)z basis set for the chloride[84] and aug-cc-pVTZ basis set for the oxygen molecule.

The investigation of the other halide-oxygen complexes has been structured to narrow down the area of concern. A suite of preliminary MP2 calculations were conducted using the Gaussian 09 program in order to refine the initial guess geometries for subsequent CCSD(T) calculations. The MP2 calculations included geometry optimisation and frequency calculations on the anion and neutral complexes and for the bare oxygen, as well as single point calculations for the bare halides and halogens and for the optimised anion geometry on the neutrals potential energy surface. All together these calculations allow values for the vertical detachment energy (VDE), the adiabatic detachment energy (ADE) as well as the dissociation energies for both the anion and neutral surfaces with and without the zero point energies being accounted for (D_e and D_o). These energies are shown in Figure 2.6 for clarity. In calculating the dissociation energies the higher X−O separation of each curve correspond to the oxygen with either the halogen or halide individually, whereas the minima represent these components as a cluster.

Each of these calculations were carried out with starting geometries of the $C_{\infty v}$, C_{2v} and C_s point groups corresponding to linear, 'Tee' and bent structures of the complex respectively. The calculations were done with correlation consistent augmented basis sets with pseudopotentials to reduce computing costs (aug-cc-pV(D, T, Q)Z-PP) sourced from the EMSL Basis Set Exchange and based on work by Dunning.[85] By using the correlation consistent basis sets developed by Dunning the results of these jobs can then be extrapolated to the complete basis set (CBS). The

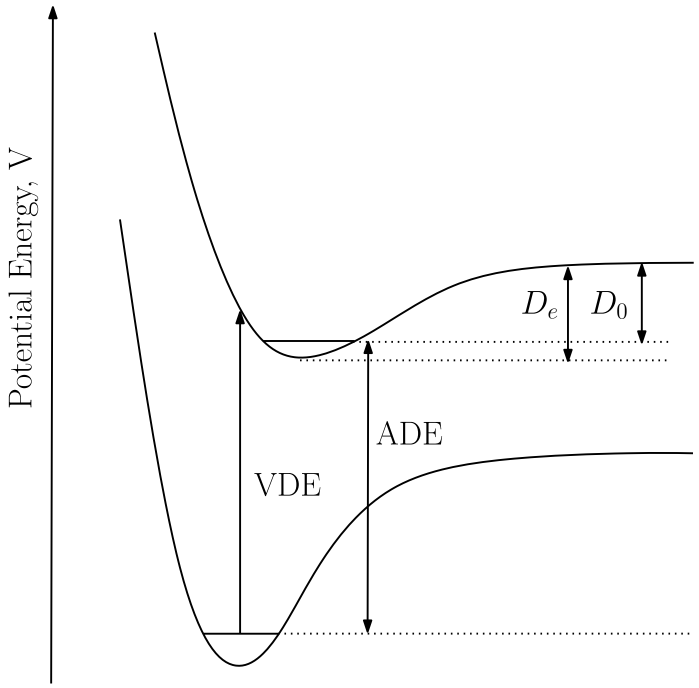

Figure 2.6: A representation of the potential energy surfaces and the energies that can be derived from them.

extrapolation is done using the following formulae:[86,87]

$$E_{CBS}^{HF} = \frac{3^{\alpha} E_3^{HF} - 2^{\alpha} E_2^{HF}}{3^{\alpha} - 2^{\alpha}} \tag{2.12}$$

$$E_{CBS}^{corr} = \frac{3^{\beta} E_3^{corr} - 2^{\beta} E_2^{corr}}{3^{\beta} - 2^{\beta}} \tag{2.13}$$

In which the subscript HF and corr refer to the Hartree-Fock and correlation energy respectively and $\alpha = 3.4$ and $\beta = 2.2$. These values were obtained by fitting equations 2.12 to the complete basis set limit and optimising the root-mean-square error for a number of simple cases. The accuracy of this method is very good with a root mean squared deviation of $5.44\,\mathrm{kJ\,mol^{-1}}$. A similar extrapolation formula can be used for CCSD(T) calculations also where the difference is $\beta = 2.4$.[87]

Use has also been made of a potential energy surface scan script written by Duncan Wild. The script produces, by calling on either Gaussian 09 or CFOUR, a series of single point calculations that can be used to explore areas of the potential energy surface. Although interpreting the plots often does not provide accurate geometry and energy minima they do offer qualitative results in that they can indicate where the minima are located, and hence which areas of the potential energy surface to focus on.

Like the MP2 calculations CCSD(T) calculations encompassing geometry optimisation and frequency analysis using finite differentials as well as other supplementary jobs were completed to give a wide variety of information regarding the two potential energy surfaces. These calculations were completed using the Cfour program and using the same basis sets as the MP2 calculations however without calculations for the quadruple zeta basis sets. Comparison was then made between the vertical detachment energies and adiabatic detachment energies calculated and the determined binding energy from experiment.

Chapter 3

Results and Discussion

This chapter covers the results obtained from the time of flight and photoelectron spectroscopy experiments as well as the related computational results. As part of the latter, issues encountered in the calculations are discussed and how these were circumvented. Comparison is drawn between experimental and computational results and with literature values for relevant halide-oxygen complexes. Also discussed are the results obtained from increasing the partial pressure of oxygen in the gas mixtures and the implications this holds for what complexes are selectively produced. Finally the results for the halide-oxygen complexes are compared with other isoelectronic systems.

3.1 Time of Flight Mass Spectrometry

Although time of flight spectra have been recorded for each day, presented here are spectra from the 8th, 15th and 29th of August 2014 which represent gas mixtures with partial pressures of O_2 of 30 kPa, 40 kPa and 100 kPa, halogen sources of dibromomethane and methyl iodide and with argon as a backing gas bringing total pressure to 450 kPa. While methyl iodide and diiodomethane are used in the production of the latter two spectra, residual dibromomethane results in some bromide signals also being present.

The spectrum with partial O_2 pressure of 30 kPa and dibromomethane as a halogen source is shown in Figure 3.1. A complete table of peak assignments is given in Appendix A and notable peaks are discussed here. The calibration peaks of mass to charge ratios 78.93, 80.91 and 126.91 correspond to the isotopes bromide-79 and bromide-81 and iodide. The calibration of these peaks has a coefficient of regression of 0.99998. For the direct purposes of these experiments, the determination of the bromide-oxygen complex peaks, interpolating between the calibration points has proven to be effective. The bromide-oxygen complex peaks are assigned to those with a mass to charge (m/z) ratio of 110.89 and 112.88 for the bromide-79 and bromide-81 isotopes respectively and these are shown in the inset of Figure 3.1.

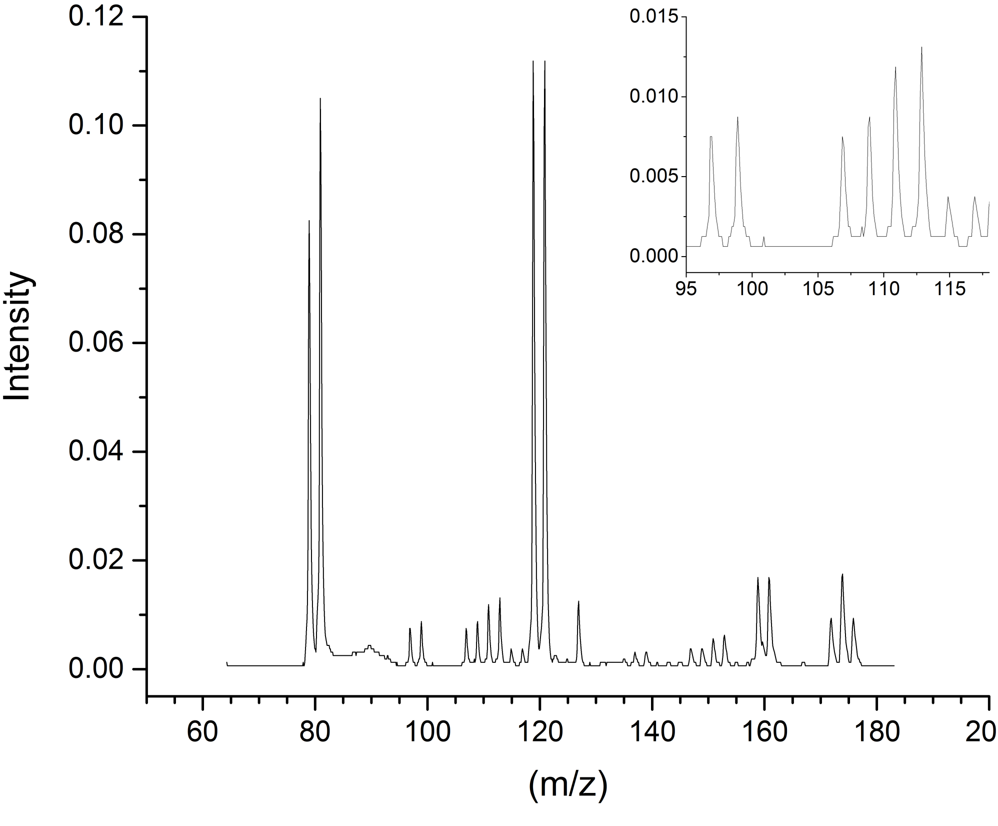

Figure 3.1: Time of flight mass spectrum of a bromide-oxygen-argon gas mixture.

Other peaks that are prominent in the spectrum those peaks with m/z ratios of 118.82 and 120.88 and are assigned to the complexes between the two bromide isotopes and argon. Often in the TOF spectra recorded, argon complexes are intense due to it being the buffer gas and maintaining at high partial pressure, in this case at least 420 kPa as the mixture is made up to 450 kPa. Initially the gas mixture is subjected to the nozzle at 450 kPa and this pressure is maintain throughout experiments by the argon backing gas. As such, over the course of experiments the original gas mixture is diluted by argon. Another interesting feature of the spectrum in Figure 3.1 is that the signal assigned to the bromide-argon complex is more intense than for the bromide-oxygen complex where usually the opposite would be expected to be the case. This is the result of tuning the sources conditions, specifically the pulse width and timing of the electron formation which favours production of one anion species over another. Overall, the strength of the signals across the spectrum has been shown to correlate with higher electron filament currents however higher currents decrease the lifetime of the filament so generally lower currents are preferred provided the signals are sufficient to produce anion species in adequate abundance to perform photoelectron spectroscopy experiments on.

As mentioned previously the inset of Figure 3.1 shows the bromide-oxygen complex peaks. Also included in this inset are a series of peaks common to many of the spectra recorded through the course of the experiments. They again appear as pairs due to the isotopic abundances of bromide and in order are bromide-water (96.88, 98.90), bromide-nitrogen (106.86, 108.92), followed by the already assigned bromide-oxygen complex and finally bromide coordinated by two water molecules (114.88, 116.91) (ie. $Br^{-}\cdots(H_2O)_2$). These complexes are likely to have arisen from atmosphere leeching into the system whether that is through some of the joints of the gas mixing apparatus or through some of the lines. These peaks may be the result of gases adsorbing onto the interior surfaces of the gas mixing station. It was seen that maintaining a positive pressure along the line from the oxygen tank to the gas mixing station and repeatedly priming and purging the station with argon to displace the adsorbed gases on the interior surfaces improved the intensity of the bromide-oxygen signal with respect to the other peaks. However provided the resolution of the spectra is high enough then the presence of these peaks is of little consequence for the photoelectron experiments. The resolution of the time of flight spectrum is determined by a definition provided by IUPAC,[88] given in equation (3.1).

$$R = \frac{M}{\Delta M} \tag{3.1}$$

Where R is the resolving power, M is the peak position and ΔM is the full width at half the maximum intensity (FWHM). Conceptually we can conceive that were there a distribution in the energies imparted to the complexes when they were accelerated the subsequent distribution in the m/z ratios based on their times of flight would be similarly spread and complexes with lower velocities (or higher masses and times of flight) would be more spread than complexes with higher velocities. This appears to be the case as a quick comparison between two example peaks from the above spectrum, the bromide-79-oxygen complex and the bromide-81-bromomethane-81 complex, have calculated resolutions of 245 and 237 respectively. This resolution is sufficient for the purposes of taking the photoelectron spectra, as there appears to be little overlap between peaks in the spectrum.

A second spectrum presented in Figure 3.2 is the methyl iodide source spectrum with a slightly higher partial pressure of O_2 of 40 kPa and again with argon as a backing gas. This spectrum was originally calibrated from 3 points and this spectrum was subsequently used to identify peaks that were then used to recalibrate the spectrum with a final calibrated spectra consisting of a 6-point calibration and coefficient of regression value of 0.98740. The three most prominent peaks that can be seen are attributed to iodide, iodide-argon and iodide-methyl iodide with peak positions of 126.92, 166.74 and 268.49 respectively (again all peaks are listed with their assignments in Appendices). This has peaks extending as far as 409.83 mass-charge ratios and demonstrates iodides larger size and more diffuse charge to bind to high degrees of micro solvation. In this case iodide-argon clusters have been assigned to have up to 7 argon atoms coordinated to an iodide anion.

The inset of Figure 3.2 shows the iodide-water (144.74) and iodide-oxygen (158.66) peaks to highlight the peak that the photoelectron spectrum is to target. There is a slight depression near a mass-charge ratio of 135 which is likely due to the saturation of the detector and appears to only have occurred for this iodide peak. Of the peaks assigned in both Figures 3.1 and 3.2 it would seem that saturation of the detector would be more likely for the bare iodide peak compared to others as it is amongst the most abundant signals and does not show any splitting due to isotopic abundances.

Another peak of interest in Figure 3.2 has a mass-charge ratio of 173.57 and has been assigned to the superoxide-methyl iodide complex and it is almost double the intensity of the iodide-oxygen complex. This raises questions as to the likely mechanism for this particular complexes formation; whether the superoxide is formed and coordinated by the methyl iodide or the methyl iodide is ionised and then coordinated by oxygen to stabilise it. The former is believed to be more likely to occur because the mechanism of formation is more simplistic and the latter mechanism involves bringing methyl iodide in an excited state of which would be expected to have a short lifetime, and the result being I^- formation from dissociative attachment. The abundance of methyl iodide in the gas mixture would mean it is difficult to produce iodide ions from all of the available methyl iodide and the higher partial pressure of O_2 would make these molecules more readily available to ionise. To investigate the ability to produce superoxide complexes another gas mixture consisting of partial pressure of O_2 of 100 kPa again with argon backing gas and with dibromomethane and diiodomethane as halide sources was made. The time of flight spectrum for this

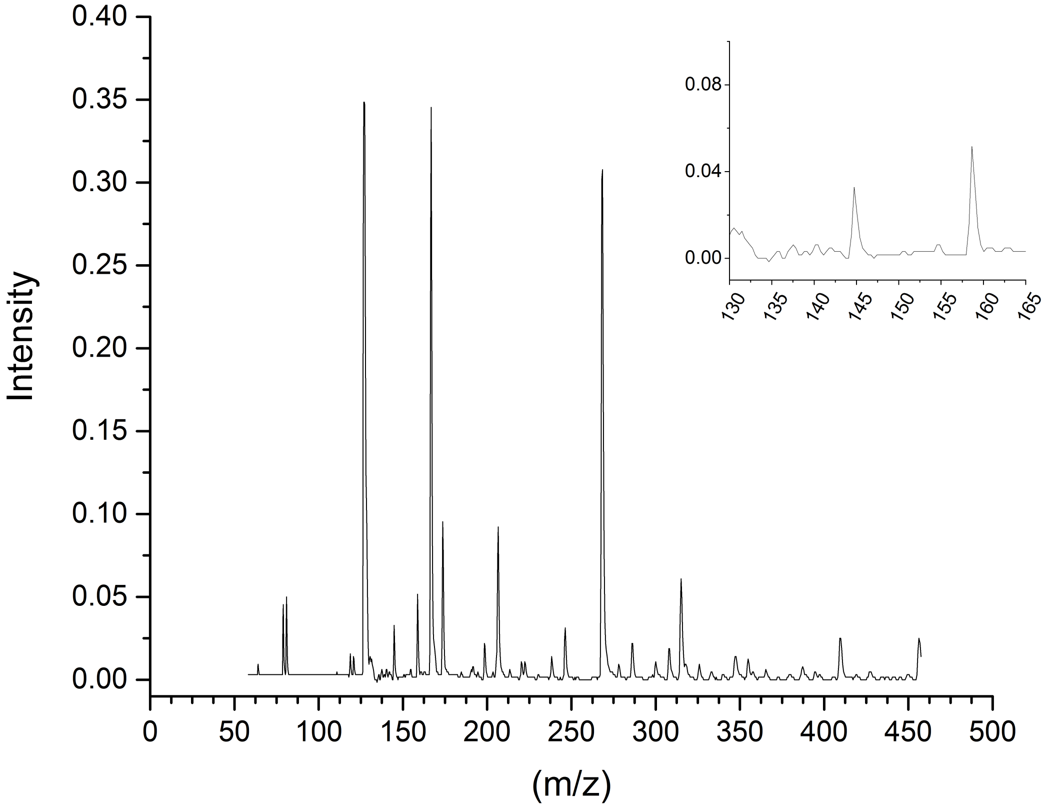

Figure 3.2: Time of flight mass spectrum of a iodide-oxygen-argon gas mixture.

mixture is shown in Figure 3.3 and peak assignments are again given in Appendix A.

In this spectrum, other than the calibration peaks of the two bromide isotopes the most notable peaks are 32.06 and 64.01 mass charge ratios and correspond to the superoxide ion and the superoxide ion coordinated further by oxygen, thereby confirming that the ion source is capable of producing O_2^-. However the most interesting peak has a mass charge ratio of 46.07 could correspond in mass to either NO_2 or CH_2O_2 and may be the Criegee intermediate, which may form through a dissociative electron attachment reaction involving methyl iodide and oxygen. If this were confirmed to be the case it would provide an avenue for further work as although Criegee intermediates have been formed in the gas phase before, experimental results are limited at the time of writing[89] and literature suggests that photoelectron spectra

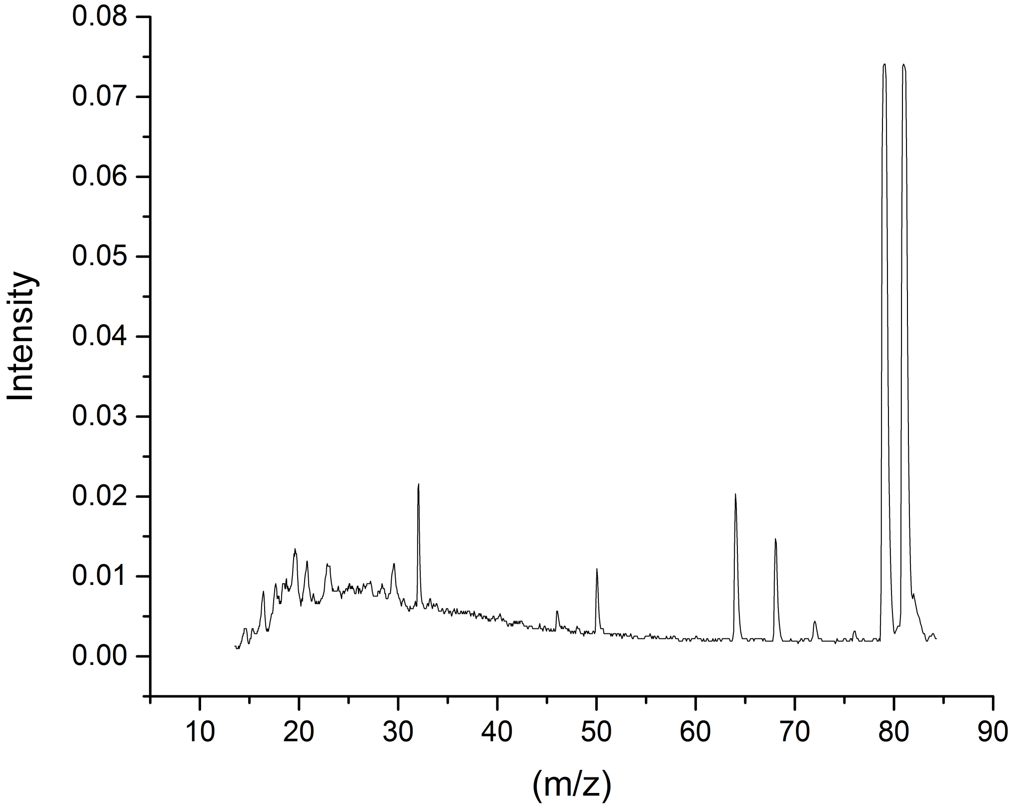

Figure 3.3: Time of flight mass spectrum to investigate superoxide complexes.

of the Criegee have not been recorded.[90] This is discussed further in Future Work.

3.2 Photoelectron Spectroscopy

Photoelectron spectra were recorded and treated using the methods detailed previously in Chapter 2. The spectra for the bromide and iodide-oxygen anion species are presented in Figures 3.4 and 3.5. These spectra also include a stick spectrum based on the results of CCSD(T) calculations, however these computational results will be discussed in more detail later. When viewing the spectra, although it is not apparent in the $^2P_{3/2}$ peak due to its higher intensity and narrower width, the $^2P_{1/2}$ shows some asymmetry. As the Jacobi applies a cubic time factor to the intensities, the tail of the peak is increased more so than the leading edge and the peak becomes more symmetric. This has implications on the reported electron binding energy of this state as the maximum often shifts to a value marginally higher in electron binding energy.

Also presented here are the electron binding energy peak values from these spectra along with those for the chloride-oxygen complex from work by Distelrath and Boesl[72] and the binding energies of the bare halogens (Table 3.1). Note that as the barycentre is given in Distelraths work, the spin-orbit splitting into the $^2P_{3/2}$ and $^2P_{1/2}$ states is calculated[91] based on the same method applied to computational results and is detailed in Appendix B. This approach uses the well known bare halogen energy levels to determine the spin-orbit coupling constant and then applying a splitting to the ab initio energy difference between anion and neutral energies.

Comparing the binding energies of the two states across the bare halides and the halide-oxygen complexes the complexes show similar splitting of the ^2P states due to spin-orbit coupling. The value of the coupling constant is greater for iodide than bromide for both the bare halides and the complexes in the spectra shown in Figures 3.4 and 3.5.

Table 3.1: Summary of experimental electron binding energies (eV)

	Cl^-		Br^-		I^-	
	$P_{3/2}$	$P_{1/2}$	$P_{3/2}$	$P_{1/2}$	$P_{3/2}$	$P_{1/2}$
Bare	3.613	3.723	3.364	3.820	3.059	4.002
Complex	3.624*	3.733*	3.432	3.904	3.118	4.056
E_{stab}	0.011	0.010	0.068	0.084	0.059	0.054

* Reference ClOO values from Boesl[72]

Also given in Table 3.1 are values for the stabilisation energy (E_{stab}), that is the difference between the electron binding energies of the halide-oxygen complexes and the halides (again note that the chloride-oxygen states are determined by the spin-orbit splitting of the bare halide and as such may not be a true reflection of

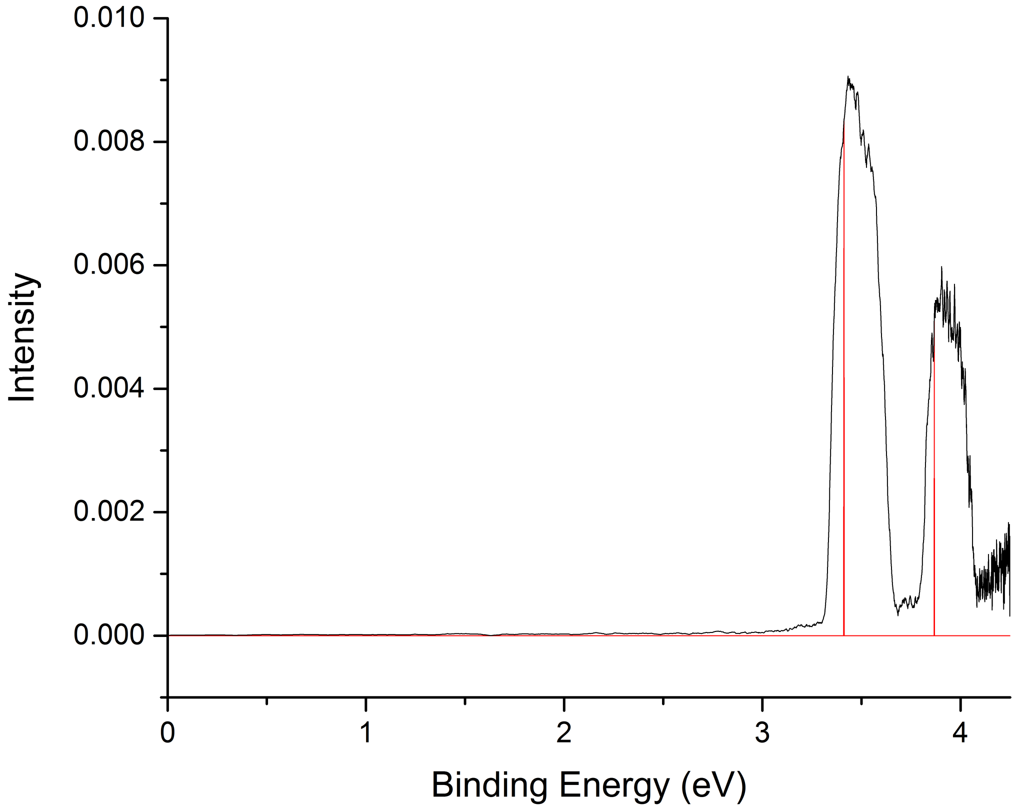

Figure 3.4: Photoelectron spectrum of bromide-oxygen complex.

these energies). In each case the electron binding energy of the complex is greater than that of the bare halide with stabilisation energies of approximately 0.01, 0.075 and 0.055 for the chloride, bromide and iodide respectively. Although the magnitude of these stabilisation energies do not appear to correlate with the size of the halides, that is provided the spin-orbit coupling of the chloride-oxygen complex is appropriately applied, these stabilisation energies being positive indicate that the coordination of the oxygen molecule to the halide has provided a stabilising effect to the system. In relation to the computational results to be discussed later the stabilisation energy should correspond to the difference in the dissociation energies (D_o) of the anion and neutral complexes. It is possible that the bromide-oxygen cluster having a comparatively higher stabilisation energy contributes to its role in atmospheric chemistry. Increased stability of the anion cluster could account for a

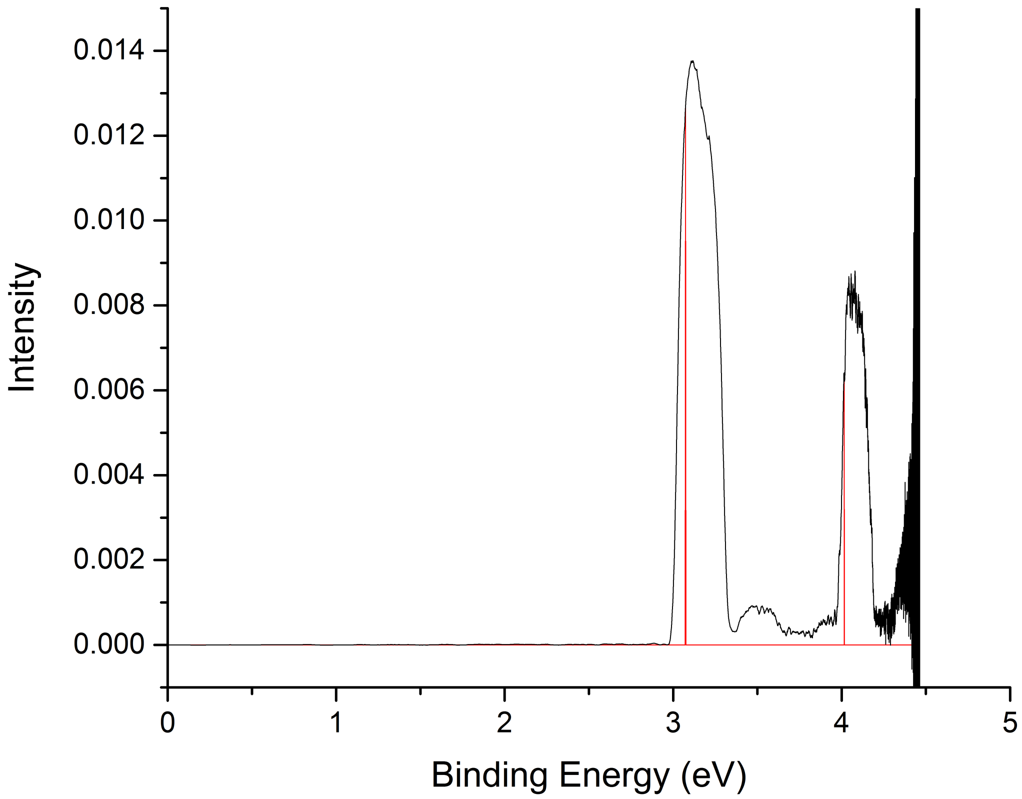

Figure 3.5: Photoelectron spectrum of iodide-oxygen complex.

longer lifetime and reactivity in the marine boundary layer and hence the formation of free bromine and subsequent coordination could lead to the degradation of ozone.

3.3 Computational Results

A series of MP2 calculations were undertaken for both the bromide and iodide complexes as well as the halides, halogens and oxygen molecule utilizing aug-cc-pVNZ-PP basis sets ($N = D, T, Q$). CCSD(T) calculations were also performed as detailed in the Methodology section. From these energy values, experimentally relevant values such as the adiabatic detachment energy (ADE) and the vertical detachment energy (VDE) were determined. All computational results are given in Appendix A, however, important results are highlighted in this section.

Following the MP2 calculations, using a starting geometry of C_s symmetry was shown to be advantageous in performing calculations on the halide-oxygen systems as the lack of restraint on the system allows it to converge to a $C_{\infty v}$ or C_{2v} symmetry if that structure indeed corresponded to the minimum energy. As such the C_s starting geometry was used for CCSD(T) calculations to reduce the number of calculations required. The structural parameters of the complexes as determined by these CCSD(T) calculations are summarised in Table 3.2.

Table 3.2: Structural parameters of the halogen-oxygen gas phase complexes predicted from CCSD(T) calculations.

	$aug-cc-pVXZ-PP$ $X = \ldots$	$r_{\mathrm{X}\cdots\parallel}$ Å	$r_{\mathrm{O-O}}$ Å	$\angle_{(\mathrm{X}-\parallel-\mathrm{O})}$ °	Point Group	Energy E_h
$Br^{-}\cdots O_2$	T	3.763	1.2135	116.70	C_s	-565.9796262
$Br\cdots O_2$	T	4.446	1.2200	180	$C_{\infty v}$	-565.8550644
$I^{-}\cdots O_2$	T	4.076	1.2141	124.02	C_s	-445.1251556
$I\cdots O_2$	T	3.501	1.2142	90	C_{2v}	-445.0078581

The values in Table 3.2 report lengths from the halide or halogen to the midpoint of the oxygen-oxygen double bond. This is used primarily to express geometry easily and consistently across point groups though it does not describe X−O bond lengths and as such they are discussed. The halide-oxygen bond lengths are shorter in the cases of $C_{\infty v}$ and C_s but longer for complexes belonging to the C_{2v} point group. Cartesian coordinates of optimized geometries are contained in Appendix A.

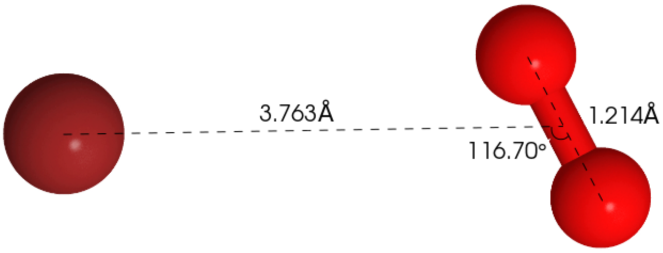

Figure 3.6: Optimised structure of BrOO anion at CCSD(T) level of theory with aug-cc-pVTZ basis sets

3.3.1 Halide-Oxygen Anion Complexes

In the cases of the bromide and iodide-O_2 anion complexes both have converged to bent structures shown in Figures 3.6 and 3.7. Determination of the harmonic frequencies indicate that both stationary points are indeed minima. Both have very similar O−O bond lengths and although there is a small difference in the bend angle present in the complex it is only 7.3°. The halide-oxygen bond length is somewhat longer in the case of iodide-oxygen being 3.771 Å for IOO^- and 3.533 Å for $BrOO^-$. This is to be expected with iodide holding an additional shell of electrons therefore is subsequently a larger ion. By comparison the difference between this two halide-oxygen bond lengths (0.238 Å) corresponds very closely to the difference between the two ionic radii (0.24 Å)[92] which suggests that both the halides are coordinated to oxygen in a similar fashion, albeit with different binding energies.

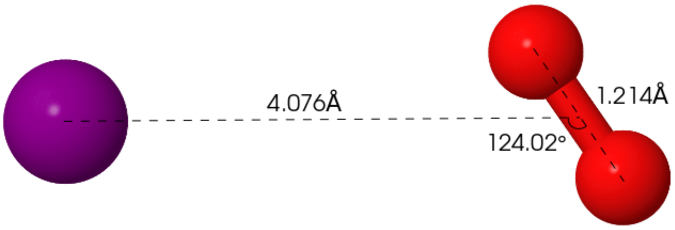

Figure 3.7: Optimised structure of IOO anion at CCSD(T) level of theory.

In describing the geometries present in the anion-oxygen complexes, electrostatic and induced multipole interactions are most suitable. The polarisabilities of the oxygen molecule are $a_{\parallel} = 15.01$ au and $a_{\perp} = 8.02$ au (au $\equiv e^2 a_0^2 E_h^{-1}$).[93] Using values from Bartolomei[94] a contour plot with separation of 25 cm^{-1} models molecular interaction taking into account charge-quadrupole, charge-hexadecapole and charge-induced dipole interactions is given in Figure 3.3.1. This agrees with the C_s symmetry found from CCSD(T) calculations and suggests that this level of multipole interaction is sufficient to qualitatively describe the complex. The optimised geometry of the anion-oxygen complexes in this model has an angle between

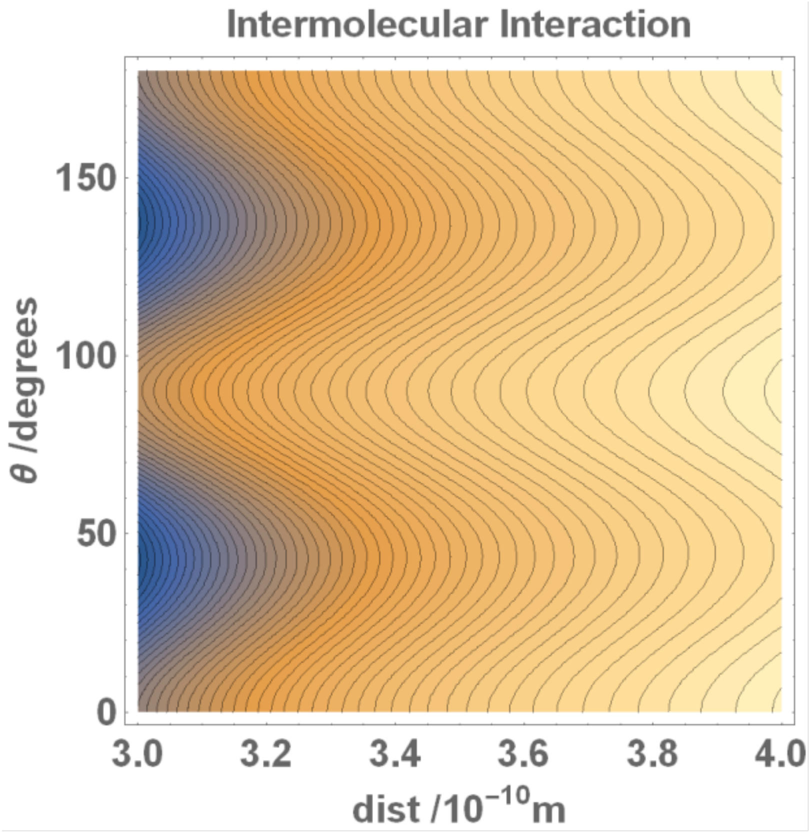

Figure 3.8: Intermolecular interaction determined for anion complexes (blue indicates stronger interaction).

the halide, the midpoint of the oxygen-oxygen double bond and the oxygen of approximately 135°. Although this model agrees with the geometries from CCSD(T) calculations it does have limitations. The electrostatic model treats the halides as a point charge and as such does not differentiate between the bromide and iodide complexes. Also as treating the halides as a point charge, it does not account for electron correlation which has been demonstrated as important in computational chemistry.

$$V_{elec}(R,\theta) = \frac{q}{4\pi\varepsilon_0}(\frac{\Theta(3\cos^2\theta - 1)}{2R^3} + \frac{\Phi(35\cos^4\theta - 30\cos^2\theta + 3)}{8R^5}) \tag{3.2}$$

$$V_{ind}(R,\theta) = -\frac{q^2(\alpha_\parallel \cos^2\theta + \alpha_\perp \sin^2\theta)}{2(4\pi\varepsilon_0)^2 R^4} \tag{3.3}$$

3.3.2 Halogen-Oxygen Neutral Complexes

In calculating the optimised structural parameters for the bromine neutral the CCSD(T) calculation converged well, to a 'Tee' structure and an energy appropriate for the complex (based on the summation of the bare halogen and oxygen molecule energies). Following calculations of the harmonic frequencies of this complex, however,gave imaginary frequencies of $43i$ and $12i$ for the intermolecular bending and stretching modes respectively which is indicative of a higher order saddle point. As the internal optimisation algorithm of CFOUR was not able to initially calculate the true minimum of the bromine complex use of the sweep script detailed in the Materials and Methods section was employed to explore the potential energy surface. Calculations were conducted by changing both the Br−X bond length and the Br−X−O angle with parameter ranges from approximately 3.69 Å to 5.09 Å in bond length with 0.1 Å intervals and 90.1° to 265.1°in bond angle with 5° intervals. Note that the angle is offset by 0.1° so that the point group is maintained as C_s throughout. The results of this sweep scan are given as a 3D plot in Figure 3.9 with the energy scale converted to kJ mol^{-1} relative to the minimum of the plot.

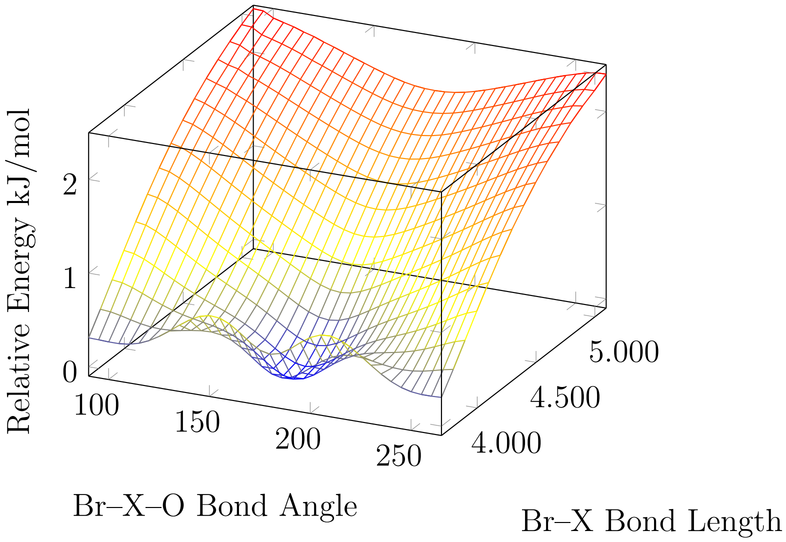

Figure 3.9: 3D plot of bromine-oxygen potential energy surface.

The scan results suggest that although a local minimum, or at least a region where the gradient is lower than convergence criteria, may be present in the 'Tee' configuration, the global minimum of this surface appears to be linear. Further sweeps were conducted along the linear configuration to report the parameters of the minima to a number of significant figures consistent with other optimised geometries and this data is then given in Table 3.2. Harmonic frequencies calculated for this geometry were found to be all real and this minimum was then confirmed as such.

Considering then the IOO neutral complex, its geometry was optimised at CCSD(T) level of theory and subsequently its vibrational frequencies were determined to confirm the geometry to be a minimum. This was completed in CFOUR and no issues arose with the results of these calculations so no potential energy surface scans needed to be conducted. By comparison to the anions this neutral complex demonstrate some unusual properties. The iodine-oxygen complex has both lower I−O and O−O bond lengths than the bromine-oxygen complex (3.553 Å and 3.836 Å respectively). This is believed to be primarily due to the iodine complex being of C_{2v} symmetry while the bromine complex is $C_{\infty v}$. In a simplistic bonding model the size of the molecule, in this case and the O−O separation, could suggest the coordination of both oxygen atoms is available to the iodine and would attract all equally. A more appropriate description of this bonding would be the interaction of the predominantly the p_x and s orbitals of the iodine with the π orbital of the oxygen molecule. In the latter description the interaction is with the double bond rather than the oxygen atoms individually.

Bromine on the other hand is of $C_{\infty v}$ symmetry as shown in Figure 3.11. The complex features a larger Br−O bond length of 3.836 Å despite its smaller atomic radius[95] which indicates a weaker interaction between the bromine and the oxygen atom. The way in which it is believed this is bonded is through the bromines p_y orbital interaction with the σ orbital of the oxygen molecule. This interaction would

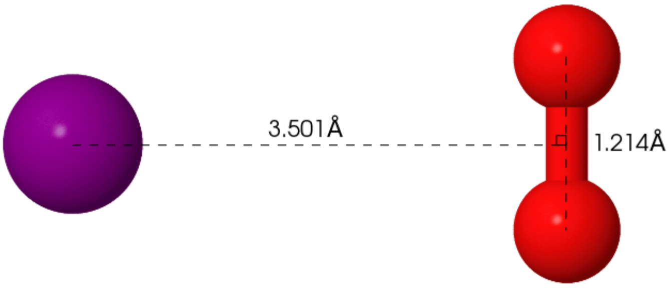

Figure 3.10: Optimised structure of IOO neutral at CCSD(T) level of theory.

also lead to a reduction in electron density from the σ bond would weaken it and lengthen the O−O bond as seen here. In both cases complex formation is deemed to be the result of dispersion interaction due to the bond lengths determined from the calculations. Both of these descriptions of orbital interaction are somewhat suitable however further calculation and analysis is required to properly describe the nature of the bonding of these complexes. This is discussed further in Future Work.

Taking into account the polarizabilites of bromine (21.8 au) and iodine (34.6 au) further explanation for the geometries of both of the neutral complexes can be given, that is, the dispersion interaction seen in these complexes.[96] The higher polarizability of iodine would suggest that the transient dipole of iodine would be greater than that of bromine. The greater dipole would be able to induce a dipole perpendicular to the bond in oxygen more so than bromine and could explain why the geometry of the iodine-oxygen complex is a 'Tee' structure and the bromine-oxygen complex is linear. Comparing the dissociation energies of the two halides (given in Table A.9), the iodine neutral complex has a significantly higer value and this indicates is a more stable.

In all calculations the anion complexes were completed on the triplet surface and the neutrals on a quartet surface. Although photodetachment of the triplet state can lead to either a doublet or a quartet state literature suggests that at higher X−O

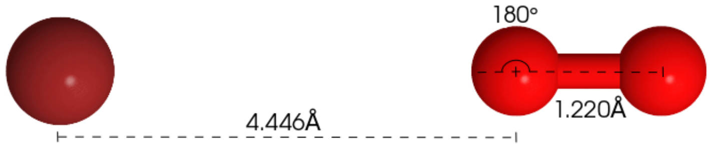

Figure 3.11: Optimised structure of BrOO neutral at CCSD(T) level of theory.

bond lengths these states become nearly degenerate.[71] Considering the resolution of the photoelectron spectra presented here, separation of these states would be difficult and as such calculations of only the quartet state is sufficient.

3.3.3 Comparison with Experimental Results

Associated energies of the optimised structures are used, along with complimentary energies of the bare halogens, halides and oxygen molecule to determine electron binding energies for comparison with experimental results. These data are summarised in Table 3.3 alongside literature values for the ClOO which includes experimental data from Boesl[72] and CCSD energy calculations by Grein.[70] Although Irikura[71] completed CCSD(T) calculations for the chloride-oxygen complex, that work does not include data for the corresponding neutral, and hence determination of the electron affinity is not possible.

In addition to accounting for the spin-orbit coupling in the electron binding energies based on the spin-orbit coupling constant taken from bare halide experimental results,[81–83] an adjustment is made to account for differences between computational and experimental results. The difference between the calculated and experimental $^2P_{3/2}$ electron binding energy for the bare halogen is defined as a shift for that level of theory and basis set. Applying this shift to the adiabatic detachment energy (ADE) of the corresponding halide-complex acts as a correction for computational values. The corrected ADE values are reported for BrOO and IOO in Table 3.3. In

Table 3.3: Summary of halide-oxygen complex electron binding energies

		ClOO Ref.*		BrOO		IOO	
		$P_{3/2}$	$P_{1/2}$	$P_{3/2}$	$P_{1/2}$	$P_{3/2}$	$P_{1/2}$
MP2	D			3.376	3.832	3.084	4.026
	T			3.382	3.839	3.082	4.024
	Q			3.385	3.841	3.081	4.023
	CBS			3.383	3.840	3.081	4.023
CCSD	T	3.7535	3.8629				
CCSD(T)	T			3.411	3.867	3.073	4.015
Experiment		3.6235	3.7329	3.432	3.904	3.118	4.056

* Reference ClOO values from Boesl[72] and Grein.[70]

general, the electron binding energies calculated are lower than experimental results but as the larger basis sets are used in MP2 calculations and following extrapolation to the complete basis set limit and then followed by CCSD(T) level values, the computational values converged towards the experimental values. This is to be expected as larger basis sets and higher levels of theory account for increasingly larger percentages of correlation interaction. Across the four CCSD(T) binding energies for the two complexes the largest difference between the corrected computational value and experiment is 0.045 eV. At this level of precision or indeed in using larger basis sets, errors in assigning the maximum intensity of the peak on the experimental spectrum is likely a larger source of error than the computational results. As such given computational results at CCSD(T) level theory and with an aug-cc-pVTZ-PP basis set of both the neutral and the anion, accurate predictions could be made as to the experimental values.

Closer inspection of the experimental spectrum for the iodide-oxygen complex reveals that there is a second peak (Figure 3.5) that has yet to be discussed. The electron binding energy of this peak is 3.492 eV and it is shifted to higher electron binding energy from the $^2P_{3/2}$ by 0.374 eV or 3017 cm^{-1}. The peak may be assigned as vibrational structure present in the spectra and the result of a transition to the $v = 1$ state of the oxygen-oxygen stretching mode in the neutral complex, which corresponds to $3136\,\mathrm{cm^{-1}}$. Due to the determination of frequencies being based on the harmonic approximation, this transition is an overestimation of the observed transition energy. Previous work done in the Wild group at UWA[15,16] investigating halide complexes with carbon monoxide again only observed vibrational structure in the case of the iodide complexes. It is suggested that other vibrational structure is either not seen due to the resolution of the photoelectron spectra being insufficient and the structure being encompassed by the $0 \leftarrow 0\ {}^2P_{3/2}$ transition or that the vibrational intensities of other transitions are below detection limits.

The dissociation energies (D_o) calculated from CCSD(T) results for the bromide, bromine, iodide and iodine complexes were 5.23, 0.71, 4.44 and 3.13 respectively (all in $\mathrm{kJ\,mol^{-1}}$). These values are similar to those derived from the preliminary MP2 calculations whose values were between approximately 3 and $6\,\mathrm{kJ\,mol^{-1}}$ (given in Appendix A).

3.3.4 Comparison with Other Isoelectronic Complexes

Comparison of the results for the halide-oxygen series with other isoelectronic species, in terms of both electron binding energy and dissociation energy is given in Table 3.4. There appears to be a consistent trend between the dissociation energies of the halide-oxygen, halide-nitrogen and halide-carbon monoxide complexes with increasing dissociation energy in that order for both of bromide and iodide. In the cases of the neutral complexes, the nitrogen complexes are approximately $0.5\,\mathrm{kJ\,mol^{-1}}$ greater than their corresponding carbon monoxide complex, which is likely due to the greater polarisability of the nitrogen molecule. The halogen-oxygen neutral complexes are lower in both cases than the other two systems but significantly lower in the bromine system which, as discussed previously, is likely the result of differences in the geometry with the oxygen complex being linear and the nitrogen complex for example being a 'Tee' shape.

Table 3.4: Comparison between halide complexes

	$P_{3/2}$	$P_{1/2}$	D_o anion	D_o neutral
BrOO	3.43	3.90	5.23	0.71
BrN_2[97]	3.44	3.88	8.8	4.0
BrCO[15]	3.50	3.97	9.9	3.5
BrNO[97]	3.51	3.96		
BrN_2O[97]	3.58	4.04		
IOO	3.12	4.06	4.44	3.13
IN_2[97]	3.15	4.01	6.5	3.8
ICO[16]	3.06	3.96	7.3	3.2
INO[97]	3.17	4.12		

In the case of bromide the electron binding energies of the complexes with nitrogen and oxygen are similar values likewise are the carbon monoxide and nitrogen monoxide complexes. This could be attributed to the coordinated molecules being homonuclear or monoxides and the implications this has to the symmetry of the complexes formed. This similarity is not seen in the monoxides for iodide and although the oxygen and nitrogen complexes still have similar electron binding energies for the $^2P_{3/2}$ state their coupling constant values differ.

Chapter 4

Conclusions and Future Work

The work discussed in this thesis aimed to investigate the halide-oxygen complexes formed with bromide and iodide through photoelectron spectroscopy and ab initio calculations. Spectra of these species were recorded using the time of flight mass spectrometer coupled to photoelectron spectrometer (TOF-PES) apparatus at UWA. Mass separation of complexes within the gas mixture prepared has been achieved with resolving power of approximately 240.

The halide-oxygen complex spectra were calibrated using known electron binding energies of bromide and iodide anions. The electron binding energies of the halide-oxygen complexes are reported as 3.432 eV, 3.904 eV and 3.118 eV, 4.056 eV for the $^2P_{3/2}$ and $^2P_{1/2}$ states in bromide-oxygen and iodide-oxygen respectively. These four electron binding energies are all greater then the corresponding electron binding energies for the bare halides with an average difference of 0.066 eV. This suggests that the coordination of oxygen in each case stabilises the halide and could have implications to the reactivity of such complexes in atmospheric reactions.

Quantum ab initio calculations were also completed to supplement experimental data. MP2 and CCSD(T) level calculations were completed using basis sets developed by Dunning.[85] The optimised geometries of these complexes were determined to be of C_s symmetry for the anion complexes in both cases and then C_{2v} and $C_{\infty v}$ for the iodine and bromine neutral complexes respectively. Electron binding energies and dissociation energies for both the anion and neutral complexes are reported and compared with other complexes and experimental results. Application of a correction based on literature values of each halide gave differences between experiment and CCSD(T) level calculations with triple zeta basis sets of less than 0.05 eV.

An appropriate model of bonding to describe the halide-oxygen complexes in these experiments are the result of electrostatic molecular interaction. Modelling of the anion interaction gives structures similar to that of CCSD(T) geometry optimisation however this model by nature fails to account for electron correlation. In the cases of the neutral halogen-oxygen complexes dispersion interaction leading to induced dipoles in the oxygen and halogen are the dominant form of interaction and the dissociation energies suggest that the iodine neutral complex is more stable that the corresponding bromine neutral complex.

Future work on these complexes could include calculations using multi-configuration self consistent field (MCSCF) theory to more accurately treat the neutral complexes given the small difference in the energies associated with the singlet and quartet surfaces.[71,98] Also completing these calculations will allow analysis of the weighting of the atomic orbitals in the make up of the molecular orbitals to be examined which may aid in the description of the nature of interaction between the halogens and oxygen molecule.

The production of superoxide anions in these experiments offers avenues for future work. At higher partial pressures of O_2 with diiodomethane as a halogen source, production of the Criegee intermediate may be possible. Current literature reports the UV absorption spectra and supplementary quantum calculations for $CH_2O_2^-$ and little experimental work investigating the structure has been completed.[89,99–101]

References

[1] Brehm, B.; Gusinow, M.; Hall, J. *Physical Review Letters* **1967**, *19*, 737–741.

[2] Boesl, U.; Knott, W. J. *Mass Spectrometry Reviews* **1998**, *17*, 275–305.

[3] Calvi, R. M.; Andrews, D. H.; Lineberger, W. C. *Chemical Physics Letters* **2007**, *442*, 12–16.

[4] Kammrath, A.; Verlet, J. R. R.; Griffin, G. B.; Neumark, D. M. *The Journal of Chemical Physics* **2006**, *125*, 1–2.

[5] Zhao, Y.; Yourshaw, I.; Reiser, G.; Arnold, C. C.; Neumark, D. M. *The Journal of Chemical Physics* **1994**, *101*, 6538–6551.

[6] Lenzer, T.; Furlanetto, M. R.; Asmis, K. R.; Neumark, D. M. *The Journal of Chemical Physics* **1998**, *109*, 10754–10766.

[7] Lenzer, T.; Yourshaw, I.; Furlanetto, M. R.; Reiser, G.; Neumark, D. M. *The Journal of Chemical Physics* **1999**, *110*, 9578–9586.

[8] Lenzer, T.; Yourshaw, I.; Furlanetto, M. R.; Pivonka, N. L.; Neumark, D. M. *The Journal of Chemical Physics* **2002**, *116*, 4170–4175.

[9] Yourshaw, I.; Lenzer, T.; Reiser, G.; Neumark, D. M. *The Journal of Chemical Physics* **1998**, *109*, 5247–5256.

[10] Jellinek, J.; Acioli, P.; Garci-Rodeja, J.; Zheng, W.; Thomas, O.; Bowen, K. *Physical Reviews B* **2006**, *74*, 1–4.

[11] Li, X.; Wang, L.-S. *The European Physical Journal D* **2005**, *34*, 9–14.

[12] Ohara, M.; Miyajima, K.; Pramann, A.; Nakajima, A.; Kaya, K. *The Journal of Physical Chemistry A* **2002**, *106*, 3702–3705.

[13] Elliott, B. M.; McCunn, L. R.; Johnson, M. A. *Chemical Physics Letters* **2008**, *467*, 32–36.

[14] Lapere, K.; LaMacchia, R.; Quak, L.; McKinley, A.; Wild, D. *Chemical Physics Letters* **2011**, *504*, 13–19.

[15] Lapere, K. M.; LaMacchia, R. J.; Quak, L. H.; Kettner, M.; Dale, S. G.; McKinley, A. J.; Wild, D. A. *Australian Journal of Chemistry* **2012**, *65*, 457–462.

[16] Lapere, K. M.; LaMacchia, R. J.; Quak, L. H.; Kettner, M.; Dale, S. G.; McKinley, A. J.; Wild, D. A. *The Journal of Physical Chemistry A* **2012**, *116*, 3577–3584.

[17] Boesl, U.; Bmann, C.; Ksmeier, R. *International Journal of Mass Spectrometry* **2001**, *206*, 231–244.

[18] Condon, E. *Physical Reviews* **1926**, *28*, 1182–1201.

[19] Skoog, D. A.; Holler, F. J.; Crouch, S. R. *Principles of Instrumental Analysis*, 6th ed.; Thomson, 2007.

[20] Bartell, L. S. *Journal of Chemical Education* **1985**, *62*, 192–196.

[21] Ellis, A.; Feher, M.; Wright, T. *Electronic and Photoelectron Spectroscopy: Fundamentals and Case Studies*; Cambridge University Press, UK, 2005.

[22] Boesl, U.; Bäßmann, C.; Drechsler, G.; Distelrath, V. *European Journal of Mass Spectrometry* **1999**, *5*, 455–470.

[23] Hirst, D. *Potential Energy Surfaces: molecular structure and reaction dynamics*; Taylor & Francis, London, 1985.

[24] Schaefer, H. *Methods of Electronic Structure Theory*; Plenum Press, New York, 1977.

[25] Lø wdin, P.-O. *Advances in Chemical Physics* **1958**, 207–322.

[26] Schrödinger, E. *Annalen der Physik* **1926**, *385*, 437–490.

[27] Jung, Y.; Lochan, R. C.; Dutoi, A. D.; Head-Gordon, M. *The Journal of Chemical Physics* **2004**, *121*, 9793–9802.

[28] Lawley, K. *Ab initio Methods in Quantum Chemistry: Part I*; John Wiley & Sons, 1977.

[29] Christiansen, O.; Olsen, J.; Jø rgensen, P.; Koch, H.; Malmqvist, P.-A. k. *Chemical Physics Letters* **1996**, *261*, 369–378.

[30] Handy, N. C.; Knowles, P. J.; Somasundram, K. *Theoretica Chimica Acta* **1985**, *68*, 87–100.

[31] Bartlett, R.; Musia, M. *Reviews of Modern Physics* **2007**, *79*, 291–352.

[32] Koch, W.; Holthausen, M. C. *A Chemist's Guide to Density Functional Theory*, 2nd ed.; Wiley-VCH, 2001.

[33] Pople, J. A. *The Journal of Chemical Physics* **1965**, *43*, S229–S230.

[34] Alcami, M.; Mó, O.; Yáñez, M.; Cooper, I. L. *The Journal of Chemical Physics* **2000**, *112*, 6131–6140.

[35] Inn, E. C. Y.; Tanaka, Y. *Journal of the Optical Society of America* **1953**, *43*, 870–873.

[36] OKeeffe, P.; Ridley, T.; Lawley, K. P. *The Journal of Chemical Physics* **2001**, *115*, 9311–9319.

[37] Krummel, P.; Fraser, P. *The 2010 Antarctic Ozone Hole Summary: Tuesday 11 January 2011*; 2011.

[38] DeMore, W. B.; Patapoff, M. *Environmental Science Technology* **1976**, *10*, 897–899.

[39] Manney, G. L.; Froidevaux, L.; Waters, J. W.; Zurek, R. W.; Read, W. G.; Elson, L. S.; Kumer, J. B.; Mergenthaler, J. L.; Roche, A. E.; ONeill, A. *Nature* **1994**, *370*, 429–434.

[40] Slaper, H.; Velders, G. J.; Matthijsen, J. *Journal of Hazardous Materials* **1998**, *61*, 77–84.

[41] Urbach, F. *Journal of Photochemistry and Photobiology B: Biology* **1997**, *40*, 3–7.

[42] McGrath, W. D.; Norrish, R. G. W. *Proceedings of the Royal Society A: Mathematical, Physical and Engineering Sciences* **1957**, *242*, 265–276.

[43] Ackerman, M.; Frimout, D.; Muller, C. *Nature* **1977**, *269*, 226–227.

[44] Molina, M. J.; Rowland, F. S. *Nature* **1974**, *249*, 810–812.

[45] Crutzen, P. *Canadian Journal of Chemistry* **1974**, *52*, 1569–1581.

[46] Solomon, S.; Garcia, R. R.; Rowland, F. S.; Wuebbles, D. J. *Nature* **1986**, *321*, 755–758.

[47] Wofsy, S. C.; McElroy, M. B. *Canadian Journal of Chemistry* **1974**, *52*, 1582–1591.

[48] Vaida, V.; Simon, J. D. *Science* **1995**, *268*, 1443–1448.

[49] Suma, K.; Sumiyoshi, Y.; Endo, Y. *The Journal of Chemical Physics* **2005**, *123*, 1–6.

[50] Wofsy, S. C.; McElroy, M. B.; Yung, Y. L. *Geophysical Research Letters* **1975**, *2*, 215–218.

[51] Salawitch, R. J. *Geophysical Research Letters* **2005**, *32*, 1–5.

[52] Butz, A.; Bsch, H.; Camy-Peyret, C.; Dorf, M.; Engel, A.; Payan, S.; Pfeilsticker, K. *Geophysical Research Letters* **2007**, *34*.

[53] Wennberg, P. *Nature* **1999**, *397*, 299–301.

[54] Avallone, L. M.; Toohey, D. W.; Schauffler, S. M.; Pollock, W. H.; Heidt, L. E.; Atlas, E. L.; Chan, K. R. *Geophysical Research Letters* **1995**, *22*, 831–834.

[55] Renard, J.-B.; Pirre, M.; Robert, C.; Huguenin, D. *Journal of Geophysical Research* **1998**, *103*, 25383–25395.

[56] Pacios, L.; Gmez, P. *Journal of Molecular Structure: THEOCHEM* **1999**, *467*, 223–231.

[57] Chase, M. W. *Journal of Physical and Chemical Reference Data* **1996**, *25*, 1069–1111.

[58] Dewar, M.; Hafner, K. *Topics in Current Chemistry: Van der Waals Systems*; Springer-Verlag, New York, 1980.

[59] Li, Z.; Jeong, G.-R. *Chemical Physics Letters* **2001**, *340*, 194–204.

[60] Alcam, M.; Cooper, I. L. *The Journal of Chemical Physics* **1998**, *108*, 9414–9424.

[61] Müller, H. S. P.; Miller, C. E.; Cohen, E. A. *The Journal of Chemical Physics* **1997**, *107*, 8292–8302.

[62] Wen, H.; Hou, G.-L.; Huang, W.; Govind, N.; Wang, X.-B. *The Journal of Chemical Physics* **2011**, *135*, 1–11.

[63] Kölm, J.; Engdahl, A.; Schrems, O.; Nelander, B. *Chemical Physics* **1997**, *214*, 313–319.

[64] Peterson, K. A. *Molecular Physics* **2010**, *108*, 393–408.

[65] Himmelmann, S.; Orphal, J.; Bovensmann, H.; Richter, A.; Ladsttter-Weissenmayer, A.; Burrows, J. P. *Chemical Physics Letters* **1996**, *251*, 330–334.

[66] Peterson, K. A.; Werner, H.-J. *The Journal of Chemical Physics* **1996**, *105*, 9823–9832.

[67] Gilles, M. K.; Polak, M. L.; Lineberger, W. C. *The Journal of Chemical Physics* **1992**, *96*, 8012–8020.

[68] Misra, A.; Marshall, P. *The Journal of Physical Chemistry A* **1998**, *102*, 9056–9060.

[69] Lee, S. Y. *The Journal of Physical Chemistry A* **2004**, *108*, 10754–10761.

[70] Grein, F. *Canadian Journal of Physics* **2011**, *89*, 891–897.

[71] Irikura, K. K. *International Journal of Mass Spectrometry* **2003**, *228*, 667–676.

[72] Distelrath, V.; Boesl, U. *Faraday Discussions* **2000**, *115*, 161–174.

[73] Seppelt, K. *Accounts of Chemical Research* **1997**, *30*, 111–113.

[74] Markovich, G.; Pollack, S.; Giniger, R.; Cheshnovsky, O. *The Journal of Chemical Physics* **1994**, *101*, 9344–9353.

[75] Proch, D.; Trickl, T. *Review of Scientific Instruments* **1989**, *60*, 713–716.

[76] van de Meerakker, S. Y. T.; Bethlem, H. L.; Meijer, G. *Nature Physics* **2008**, *4*, 595–602.

[77] Elioff, M. S. *Science* **2003**, *302*, 1940–1943.

[78] Christen, W.; Rademann, K. *Physical Reviews A* **2008**, *77*, 1–5.

[79] Cheshnovsky, O.; Yang, S. H.; Pettiette, C. L.; Craycraft, M. J.; Smalley, R. E. *Review of Scientific Instruments* **1987**, *58*, 2131–2137.

[80] Kruit, P.; Read, F. H. *Journal of Physics E: Scientific Instruments* **1983**, *16*, 313–324.

[81] Blondel, C.; Cacciani, P.; Delsart, C.; Trainham, R. *Physical Reviews A* **1989**, *40*, 3698–3701.

[82] Luc-Koenig, E.; Morillon, C.; Vergs, J. *Physica Scripta* **1975**, *12*, 199–219.

[83] Peláez, R. J.; Blondel, C.; Delsart, C.; Drag, C. *Journal of Physics B: Atomic, Molecular and Optical Physics* **2009**, *42*, 1–7.

[84] Dunning, T. H.; Peterson, K. A.; Wilson, A. K. *The Journal of Chemical Physics* **2001**, *114*, 9244–9253.

[85] Dunning, T. H. *The Journal of Chemical Physics* **1989**, *90*, 1007–1023.

[86] Scheiner, S. *Computational and Theoretical Chemistry* **2012**, *998*, 9–13.

[87] Truhlar, D. G. *Chemical Physics Letters* **1998**, *294*, 45–48.

[88] McNaught, A.; Wilkinson, A. *IUPAC Compendium of Chemical Terminology*, 2nd ed.; Blackwell Scientific Publications, 1997.

[89] Karton, A.; Kettner, M.; Wild, D. *Chemical Physics Letters* **2013**, *585*, 15–20.

[90] Welz, O.; Savee, J. D.; Osborn, D. L.; Vasu, S. S.; Percival, C. J.; Shallcross, D. E.; Taatjes, C. A. *Science* **2012**, *335*, 204–207.

[91] Atkins, P.; de Paula, J. *Atkins' Physical Chemistry*, 9th ed.; Oxford University Press, 2010.

[92] Shannon, R. D. *Acta Crystallogr Sect A Cryst Phys Diffr Theor Gen Crystallogr* **1976**, *32*, 751–767.

[93] Medved, M.; Urban, M.; Kell, V.; Diercksen, G. H. *Journal of Molecular Structure: THEOCHEM* **2001**, *547*, 219–232.

[94] Bartolomei, M.; Carmona-Novillo, E.; Hernndez, M. I.; Campos-Martnez, J.; Hernndez-Lamoneda, R. *Journal of Computational Chemistry* **2010**, *32*, 279–290.

[95] Slater, J. C. *The Journal of Chemical Physics* **1964**, *41*, 3199–3204.

[96] Fleig, T.; Sadlej, A. J. *Phys. Rev. A* **2002**, *65*.

[97] Lapere, K. Anion Photoelectron Spectroscopy of Halide Complexes and Clusters. Ph.D. thesis, University of Western Australia: School of Chemistry and Biochemistry, 2014.

[98] Schmidt, M. W.; Gordon, M. S. *Annual Review of Physical Chemistry* **1998**, *49*, 233–266.

[99] Beames, J. M.; Liu, F.; Lu, L.; Lester, M. I. *Journal of the American Chemical Society* **2012**, *134*, 20045–20048.

[100] Dawes, R.; Jiang, B.; Guo, H. *Journal of the American Chemical Society* **2015**, *137*, 50–53.

[101] Sheps, L. *The Journal of Physical Chemistry Letters* **2013**, *4*, 4201–4205.

Appendix A

Tables and Data

In the following tables the basis sets are often abbreviated to D, T or Q which correspond to the aug-cc-pV(D,T or Q)Z-PP basis sets. $r_{\mathrm{X}\cdots\|}$ corresponds to the distance between the halide and the midpoint of the oxygen-oxygen double bond and $\angle_{(\mathrm{X}-\|-\mathrm{O})}$ represents the angle this makes with the oxygen-oxygen double bond.

Table A.1: Energies of the bare halogens (all in Hartrees)

MP2	Br^-	Br	I^-	I
D	−415.7141766	−415.5906193	−294.8722779	−294.7554165
T	−415.8182646	−415.6917550	−294.9658305	−294.8458971
Q	−415.8967867	−415.7667885	−295.0462741	−294.9223505
CBS	−415.8855922	−415.7559038	−295.0291381	−294.9058109
CCSD(T)				
T	−415.8364248	−415.7132791	−294.9822876	−294.8654129

Table A.2: Geometries and energies of oxygen molecule

MP2	$r_{\mathrm{O-O}}$ Å	E_h Hartree	zpe $\mathrm{kJ\,mol^{-1}}$	ω_1
D	1.2337	−150.0042898	8.54	1428 (σ_g^+) **0**
T	1.2244	−150.1209379	8.70	1455 (σ_g^+) **0**
Q	1.2189	−150.1604304	8.85	1480 (σ_g^+) **0**
CBS		−150.1884398	Assignment:	O−O stretch
CCSD(T)				
T	1.213	−150.1410200	9.42	1574 (σ_g^+) **0**

Table A.3: Structural parameters of the halogen-oxygen neutral gas phase complexes predicted from calculations.

	Starting Point Group	Basis Set	$r_{\mathrm{X}\cdots\Vert}$ Å	$r_{\mathrm{O-O}}$ Å	$\angle_{(\mathrm{X}-\Vert-\mathrm{O})}$ °	Change in Point Group	Energy E_h
MP2							
$\mathrm{Br}\cdots\mathrm{O}_2$	C_{2v}	D	3.359	1.2351	90		-565.5962152
		T	3.238	1.2259	90		-565.8142361
		Q	3.219	1.2205	90		-565.9288910
		CBS*					-565.9463034
	$C_{\infty v}$	D	3.872	1.2335	180		-565.5961980
		T	3.768	1.2244	180		-565.8141808
		Q	3.732	1.2189	180		-565.9288910
		CBS*					-565.9461384
	C_s	D	3.359	1.2351	90	C_{2v}	-565.5962152
		T	3.238	1.2259	90	C_{2v}	-565.8142361
		Q	3.219	1.2205	90	C_{2v}	-565.9288922
		CBS*					-565.9463034
$\mathrm{I}\cdots\mathrm{O}_2$	C_{2v}	D	3.624	1.2349	90		-444.7609698
		T	3.445	1.2259	90		-444.9685180
		Q	3.440	1.2205	90		-445.0846410
		CBS*					-445.0965597
	$C_{\infty v}$	D	4.546	1.2339	180		-444.7605982
		T	4.418	1.2250	180		-444.9677770
		Q	4.406	1.2196	180		-445.0838421
		CBS*					-445.0953995
	C_s	D	3.625	1.2349	90	C_{2v}	-444.7609697
		T	3.445	1.2259	90	C_{2v}	-444.9685180
		Q	3.880	1.2190	90	C_{2v}	-445.0840305
		CBS*					-445.0965597
CCSD(T)							
$\mathrm{Br}\cdots\mathrm{O}_2$	N/A	T	4.446	1.2200	180	$C_{\infty v}$	-565.8550644
$\mathrm{I}\cdots\mathrm{O}_2$	C_s	T	3.501	1.2142	90	C_{2v}	-445.0078581

* CBSL = Complete basis set limit derived from two point extrapolation.

Table A.4: Structural parameters of the halogen-oxygen anion gas phase complexes predicted from calculations.

	Starting Point Group	Basis Set	$r_{\mathrm{X}\cdots\parallel}$ Å	$r_{\mathrm{O-O}}$ Å	$\angle_{(\mathrm{X}-\parallel-\mathrm{O})}$ °	Change in Point Group	Energy E_h
MP2							
$\mathrm{Br}^{-}\cdots \mathrm{O}_2$	C_{2v}	D	3.803	1.2327	90		-565.7202850
		T	3.651	1.2235	90		-565.9414731
		Q	3.615	1.2181	90		-566.0596963
		CBS^{*}					-566.0767436
	$C_{\infty v}$	D	4.258	1.2356	180		-565.7203308
		T	4.192	1.2265	180		-565.9410292
		Q	4.141	1.2212	180		-566.0590934
		CBS^{*}					-566.0759982
	C_s	D	3.803	1.2327	90	C_{2v}	-565.7202850
		T	3.651	1.2235	90	C_{2v}	-565.9414731
		Q	3.615	1.2181	90	C_{2v}	-566.0596964
		CBS^{*}					-566.0767436
$\mathrm{I}^{-}\cdots \mathrm{O}_2$	C_{2v}	D	4.104	1.2329	90		-444.8781078
		T	3.911	1.2238	90		-445.0887335
		Q	3.884	1.2184	90		-445.2090019
		CBS^{*}					-445.2200173
	$C_{\infty v}$	D	4.549	1.2353	180		-444.8781951
		T	4.419	1.2264	180		-445.0884184
		Q	4.414	1.2210	180		-445.2084782
		CBS^{*}					-445.2194510
	C_s	D	4.104	1.2329	90	C_{2v}	-444.8781078
		T	3.911	1.2238	90	C_{2v}	-445.0887335
		Q	3.884	1.2181	90	C_{2v}	-445.2090019
		CBS^{*}					-445.2200173
CCSD(T)							
$\mathrm{Br}^{-}\cdots \mathrm{O}_2$	C_s	T	3.763	1.2135	116.70		-565.9796262
$\mathrm{I}^{-}\cdots \mathrm{O}_2$	C_s	T	4.076	1.2141	124.02		-445.1251556

[*] CBSL = Complete basis set limit derived from two point extrapolation.

Table A.5: Cartesian coordinates of the CCSD(T)/aug-cc-pVTZ-PP optimised geometries for the halide-oxygen and halogen-oxygen complexes in Å.

Atom/Ion	x	y	z
Br^-	1.085372082	0.016265305	0.000000000
O	-2.396874149	-0.578007037	0.000000000
O	-2.958312853	0.497754614	0.000000000
Br	0.000000000	0.000000000	-1.282451675
O	0.000000000	0.000000000	2.553801270
O	0.000000000	0.000000000	3.773769368
I^-	-0.820701165	-0.010674145	0.000000000
O	2.909577761	0.540995666	0.000000000
O	3.601907378	-0.456306436	0.000000000
I	0.000000000	0.000000000	-0.704802505
O	0.000000000	0.607105452	2.795969607
O	0.000000000	-0.607105452	2.795969602

Table A.6: MP2 Harmonic Frequencies. Frequencies are in cm^{-1}, intensities are in m mol^{-1}, also provided are mode symmetries

MP2 (aug-cc-pVDZ-PP)	Point Group	$C_{\infty v}$	C_{2v}	C_s
$\mathrm{Br^-}\cdots\mathrm{O_2}$	ω_1	1445 σ^+ **4704**	1433 a_1 **7**	
	ω_2	40 σ^+ **4016**	40 a_1 **3626**	
	ω_3	34 π **566**	171 b_2 **153**	
$\mathrm{Br}\cdots\mathrm{O_2}$	ω_1	1429 σ^+ **331**	1421 a_1 **110**	
	ω_2	44 σ^+ **74**	43 a_1 **676**	
	ω_3	39 π **2**	150 b_2 **79**	
$\mathrm{I^-}\cdots\mathrm{O_2}$	ω_1	1440 σ^+ **3865**	1431 a_1 **1**	
	ω_2	34 σ^+ **1651**	33 a_1 **1469**	
	ω_3	31 π **281**	126 b_2 **219**	
$\mathrm{I}\cdots\mathrm{O_2}$	ω_1	1523 σ^+ **76**	1421 a_1 **94**	
	ω_2	30 σ^+ **10**	39 a_1 **72**	
	ω_3	32 π **< 1**	129 b_2 **498**	

MP2 (aug-cc-pVTZ-PP)	Point Group	$C_{\infty v}$	C_{2v}	C_s
$\mathrm{Br^-}\cdots\mathrm{O_2}$	ω_1	1466 σ^+ **2944**	1458 a_1 **25**	
	ω_2	42 σ^+ **4007**	46 a_1 **3614**	
	ω_3	10 π **602**	143 b_2 **62**	
$\mathrm{Br}\cdots\mathrm{O_2}$	ω_1	1453 σ^+ **344**	1446 a_1 **126**	
	ω_2	48 σ^+ **99**	52 a_1 **112**	
	ω_3	34 π **4**	125 b_2 **96**	
$\mathrm{I^-}\cdots\mathrm{O_2}$	ω_1	1462 σ^+ **2363**	1456 a_1 **14**	
	ω_2	37 σ^+ **1595**	39 a_1 **1397**	
	ω_3	6i π **325**	112 b_2 **144**	
$\mathrm{I}\cdots\mathrm{O_2}$	ω_1	1479 σ^+ **113**	1446 a_1 **105**	
	ω_2	34 σ^+ **13**	50 a_1 **128**	
	ω_3	20 π **< 1**	118 b_2 **95**	

MP2 (aug-cc-pVQZ-PP)	Point Group	$C_{\infty v}$	C_{2v}	C_s
$\mathrm{Br^-}\cdots\mathrm{O_2}$	ω_1	1487 σ^+ **1922**	1482 a_1 **31**	
	ω_2	45 σ^+ **3961**	49 a_1 **3557**	
	ω_3	13i π **648**	116 b_2 **29**	
$\mathrm{Br}\cdots\mathrm{O_2}$	ω_1	1478 σ^+ **323**	1470 a_1 **134**	
	ω_2	54 σ^+ **115**	55 a_1 **124**	
	ω_3	41 π **5**	110 b_2 **32**	
$\mathrm{I^-}\cdots\mathrm{O_2}$	ω_1	1484 σ^+ **1553**	1481 a_1 **18**	
	ω_2	37 σ^+ **1599**	43 a_1 **1380**	
	ω_3	14i π **345**	89 b_2 **84**	
$\mathrm{I}\cdots\mathrm{O_2}$	ω_1	1485 σ^+ **130**	1470 a_1 **107**	
	ω_2	33 σ^+ **13**	48 a_1 **131**	
	ω_3	19 π **< 1**	99 b_2 **35**	

Table A.7: CCSD(T) Harmonic Frequencies. Frequencies are in cm^{-1}, intensities are in m mol^{-1}, also provided are mode symmetries

CCSD(T) (aug-cc-pVTZ-PP)	Point Group	$C_{\infty v}$	C_{2v}	C_s
$Br^{-}\cdots O_2$	ω_1			1587 a' **2995**
	ω_2			50 a' **5102**
	ω_3			20 a' **127**
$Br\cdots O_2$	ω_1	1536 σ^+ **109**		
	ω_2	22 σ^+ **1**		
	ω_3	117 π **16**		
$I^{-}\cdots O_2$	ω_1			1578 a' **4553**
	ω_2			46 a' **2400**
	ω_3			20 a' **126**
$I\cdots O_2$	ω_1		1568 a_1 **207**	
	ω_2		46 a_1 **107**	
	ω_3		63 b_2 **4**	
Mode Assignments				
	ω_1	O−O stretch	O−O stretch	O−O stretch
	ω_2	X−O stretch	X− $\parallel$ stretch	X−O stretch
	ω_3	X−O−O bend	O−O rock	X−O−O bend

Table A.8: Important energies of the halogen-oxygen anion gas phase complexes predicted from calculations.

		Basis Set	zpe kJ mol^{-1}	D_e kJ mol^{-1}	D_o kJ mol^{-1}	VDE eV
MP2						
$Br^{-} \cdots O_2$	C_{2v}	D	9.83	4.77	6.06	3.282
		T	9.85	5.96	7.11	3.370
		Q	9.85	6.51	7.51	3.468
		CBS/Q				3.462*
	$C_{\infty v}$	D	9.28	4.89	5.64	3.480
		T	9.14	4.80	5.24	3.460
		Q	9.16	4.93	5.24	3.554
		CBS/Q				3.453*
$I^{-} \cdots O_2$	C_{2v}	D	9.52	4.04	5.02	3.101
		T	9.61	5.16	6.07	3.191
		Q	9.65	6.03	6.83	3.302
		CBS/Q				3.287*
	$C_{\infty v}$	D	9.18	4.27	4.91	3.105
		T	8.97	4.33	4.60	3.190
		Q	9.10	4.66	4.90	3.297
		CBS/Q				3.282*
CCSD(T)						
$Br^{-} \cdots O_2$	C_s	T	9.91	5.73	5.23	3.287
$I^{-} \cdots O_2$	C_s	T	9.83	4.85	4.44	3.090

* VDE values calculated with CBS energies and pvqz zero-point energy.

Table A.9: Important energies of the halogen-oxygen neutral gas phase complexes predicted from calculations.

		Basis Set	zpe kJ mol^{-1}	D_e kJ mol^{-1}	D_o kJ mol^{-1}	ADE eV
MP2						
Br$\cdots$O$_2$	C_{2v}	D	9.65	3.43	4.54	3.374
		T	9.71	4.05	5.06	3.460
		Q	9.78	4.39	5.32	3.559
		CBS/Q				3.549*
	$C_{\infty v}$	D	9.28	3.38	4.12	3.378
		T	9.38	3.91	4.59	3.454
		Q	9.66	4.39	5.19	3.548
		CBS/Q				3.539*
I$\cdots$O$_2$	C_{2v}	D	9.50	3.32	4.27	3.187
		T	9.65	4.42	5.37	3.272
		Q	9.67	4.88	5.71	3.384
		CBS/Q				3.360*
	$C_{\infty v}$	D	9.67	2.34	3.46	3.205
		T	9.28	2.47	3.05	3.286
		Q	9.30	2.79	3.24	3.394
		CBS/Q				3.378*
CCSD(T)						
Br$\cdots$O$_2$	$C_{\infty v}$	T	10.72	2.01	0.71	3.398
I$\cdots$O$_2$	C_{2v}	T	10.03	3.74	3.13	3.194

* ADE values calculated with CBS energies and pvqz zero-point energies.

Table A.10: Calculation of energy shift constants in eV

MP2	Br VDE	Split $P_{3/2}$	Split $P_{1/2}$	Ref*	$P_{3/2}$ Shift
D	3.3621	3.2099	3.6665	3.3636	-0.1537
T	3.4424	3.2902	3.7468		-0.0734
Q	3.5373	3.3851	3.8417		0.0216
CBS	3.5289	3.3767	3.8333		0.0131
	I VDE				
D	3.1799	2.8659	3.8079	3.0590	-0.1931
T	3.2635	2.9495	3.8915		-0.1095
Q	3.3720	3.0580	4.0001		-0.0010
CBS	3.3558	3.0418	3.9838		-0.0172
CCSD(T)	Br VDE				
T	3.3509	3.1987	3.6553	3.3636	-0.1649
	I VDE				
T	3.1802	2.8662	3.8083	3.059	-0.1928

* Reference $P_{3/2}$ values from NIST[81–83]

Table A.11: Application of spin-orbit splitting and shifts to calculated BrOO ADE values in eV

MP2	$C_{\infty v}$	Split $P_{3/2}$	Split $P_{1/2}$	Shifted $P_{3/2}$	Shifted $P_{1/2}$
D	3.3777	3.2255	3.6821	3.3792	3.8358
T	3.4542	3.3020	3.7586	3.3753	3.8319
Q	3.5480	3.3958	3.8524	3.3743	3.8309
CBS	3.5387	3.3865	3.8431	3.3734	3.8300
	C_{2v}				
D	3.3742	3.2220	3.6786	3.3757	3.8323
T	3.4608	3.3086	3.7652	3.3820	3.8386
Q	3.5586	3.4064	3.8630	3.3848	3.8414
CBS	3.5487	3.3965	3.8531	3.3833	3.8399
CCSD(T)					
T	3.3979	3.2457	3.7023	3.4106	3.8672

Table A.12: Application of spin-orbit splitting and shifts to calculated IOO ADE values in eV

MP2	$C_{\infty v}$	Split $P_{3/2}$	Split $P_{1/2}$	Shifted $P_{3/2}$	Shifted $P_{1/2}$
D	3.2049	2.8909	3.8329	3.0840	4.0261
T	3.2860	2.9720	3.9141	3.0816	4.0236
Q	3.3936	3.0796	4.0216	3.0805	4.0225
CBS	3.3777	3.0636	4.0057	3.0808	4.0229
	C_{2v}				
D	3.1872	2.8732	3.8153	3.0664	4.0084
T	3.2716	2.9576	3.8996	3.0671	4.0091
Q	3.3842	3.0702	4.0123	3.0712	4.0132
CBS	3.3597	3.0457	3.9877	3.0629	4.0049
CCSD(T)					
T	3.1939	2.8799	3.8219	3.0727	4.0147

Table A.13: Peak positions and assignments in dibromomethane-oxygen mix

Position (m/z)	Assignment
78.93	$^{79}Br^{-}$
80.91	$^{81}Br^{-}$
96.88	$^{79}Br^{-} \cdots (H_2O)$
98.90	$^{81}Br^{-} \cdots (H_2O)$
106.86	$^{79}Br^{-} \cdots (N_2)$
108.92	$^{81}Br^{-} \cdots (N_2)$
110.89	$^{79}Br^{-} \cdots (O_2)$
112.88	$^{81}Br^{-} \cdots (O_2)$
114.88	$^{79}Br^{-} \cdots 2\,(H_2O)$
116.91	$^{81}Br^{-} \cdots 2\,(H_2O)$
118.82	$^{79}Br^{-} \cdots Ar$
120.88	$^{81}Br^{-} \cdots Ar$
126.91	$^{127}I^{-}$
136.93	$^{79}Br^{-} \cdots Ar(H_2O)$
138.94	$^{81}Br^{-} \cdots Ar(H_2O)$
146.86	$^{79}Br^{-} \cdots Ar(N_2)$
148.88	$^{81}Br^{-} \cdots Ar(N_2)$
150.84	$^{79}Br^{-} \cdots Ar(O_2)$
152.88	$^{81}Br^{-} \cdots Ar(O_2)$
158.81	$^{79}Br^{-} \cdots 2\,(Ar)$
160.77	$^{81}Br^{-} \cdots 2\,(Ar)$
171.88	$^{79}Br_2CH_2^{-}$
173.91	$^{79}Br^{81}BrCH_2^{-}$
175.81	$^{81}Br_2CH_2^{-}$

Table A.14: Peak positions and assignments in iodomethane-oxygen mix

Position (m/z)	Assignment
64.11	$O_2^- \cdots (O_2)$
79.01	$^{79}Br^-$
80.98	$^{81}Br^-$
118.83	$^{79}Br^- \cdots Ar$
120.64	$^{81}Br^- \cdots Ar$
126.92	$^{127}I^-$
144.74	$^{127}I^- \cdots (H_2O)$
158.66	$^{127}I^- \cdots (O_2)$
166.74	$^{127}I^- \cdots Ar$
173.57	$O_2^- \cdots (CH_3I)$
198.36	$^{127}I^- \cdots Ar(O_2)$
206.60	$^{127}I^- \cdots 2\,(Ar)$
220.29	$^{79}Br^- \cdots (CH_3I)$
222.34	$^{81}Br^- \cdots (CH_3I)$
238.23	$^{127}I^- \cdots 2\,(Ar)(O_2)$
246.38	$^{127}I^- \cdots 3\,(Ar)$
268.49	$^{127}I^- \cdots (CH_3I)$
278.05	$^{127}I^- \cdots 3\,(Ar)(O_2)$
286.15	$^{127}I^- \cdots 4\,(Ar)$
300.07	$^{127}I^- \cdots (CH_3I)(O_2)$
308.00	$^{127}I^- \cdots Ar(CH_3I)$
315.06	$O_2^- \cdots 2\,(CH_3I)$
325.91	$^{127}I^- \cdots 5\,(Ar)$
354.89	$^{127}I^- \cdots 5\,(Ar)(N_2)$
365.35	$^{127}I^- \cdots 6\,(Ar)$
409.83	$^{127}I^- \cdots 7\,(Ar)$

Table A.15: Peak positions and assignments in dibromomethane-oxygen (100kPa) mix

Position (m/z)	Assignment
32.06	O_2^-
46.07	$O_2^- \cdots (CH_2)$ or NO_2^-
50.04	$O_2^- \cdots (H_2O)$
64.01	$O_2^- \cdots (O_2)$
68.01	$O_2^- \cdots 2\,(H_2O)$
72.01	$O_2^- \cdots Ar$
76.09	$O_2^- \cdots (NO_2)$
79.00	$^{79}Br^-$
80.98	$^{81}Br^-$

Appendix B

Additional Appendices

B.1 Calculations of Coupling Constants

$$E_{\ell,s,j} = \frac{1}{2}hc\widetilde{A}(j(j+1) - \ell(\ell+1) - s(s+1))$$

$$hc = 1.239 \times 10^{-4}\,\text{eV}\,\text{cm}$$

$$\ell = 1, s = \frac{1}{2}, j = \frac{1}{2}, \frac{3}{2}$$

$$E_{j=\frac{1}{2}} = \frac{1}{2}hc\widetilde{A}(\frac{3}{4} - 2 - \frac{3}{4})$$

$$E_{j=\frac{3}{2}} = \frac{1}{2}hc\widetilde{A}(\frac{15}{4} - 2 - \frac{3}{4})$$

$$E_{j=\frac{1}{2}} - E_{j=\frac{3}{2}} = \frac{-3}{2}hc\widetilde{A}$$

$$\Delta E_{Cl} = 0.1094\,\text{eV} \Rightarrow \widetilde{A} = -588.65\,\text{cm}^{-1}$$

$$\Delta E_{Br} = 0.4569\,\text{eV} \Rightarrow \widetilde{A} = -2456.82\,\text{cm}^{-1}$$

$$\Delta E_{I} = 0.9426\,\text{eV} \Rightarrow \widetilde{A} = -5068.76\,\text{cm}^{-1}$$

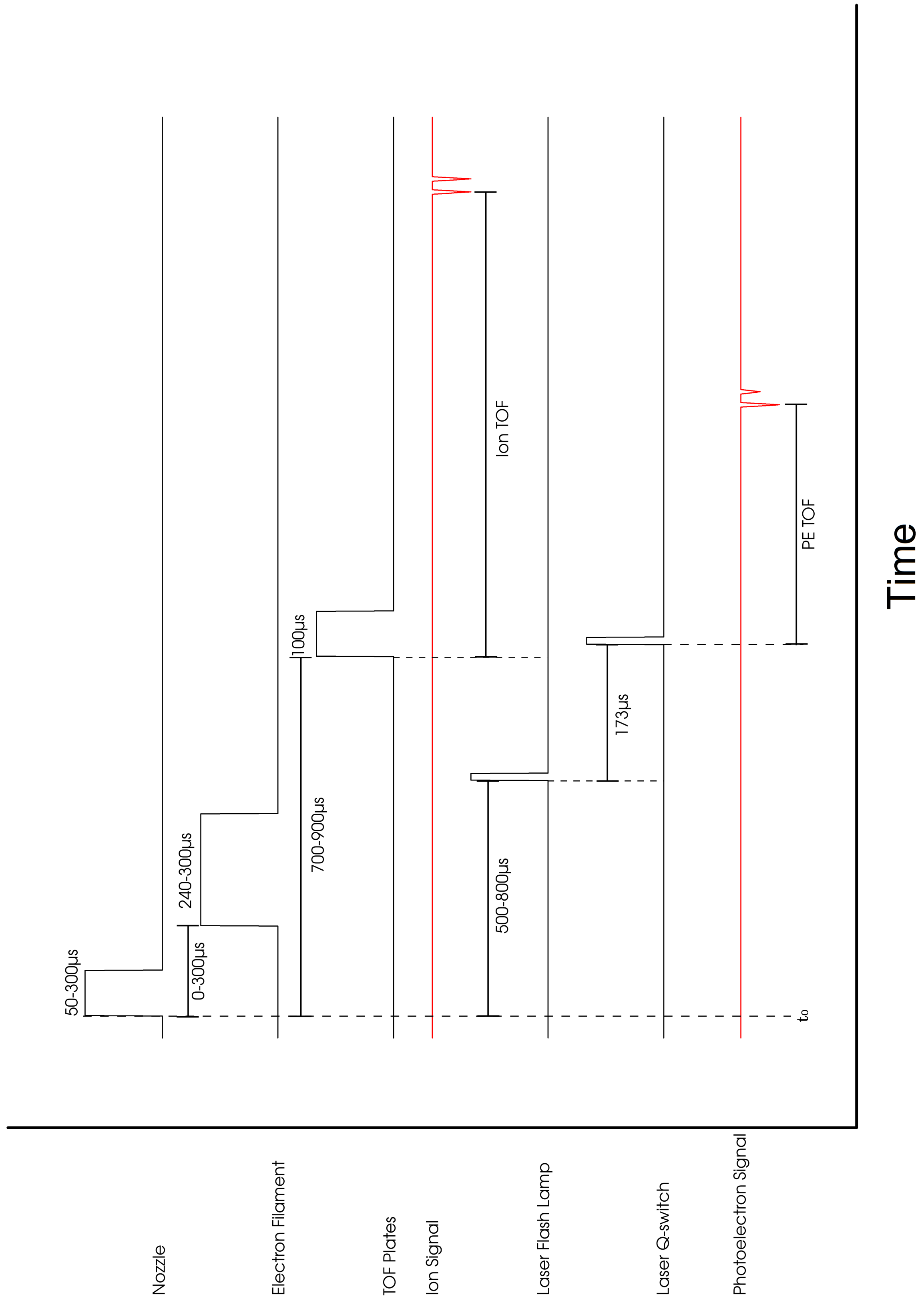

Figure B.1: Diagram showing the times of different pulsed apparatus used in experiments.